CHEMISTRY

Ultrafast, remote-controlled protonation reaction enables structural changes in a phytochrome

Madan Kumar Shankar[1,2,3]†, Lukas Grunewald[2]†, Weixiao Yuan Wahlgren[1,4]†, Brigitte Stucki-Buchli[5], Amke Nimmrich[1,6], Moona Kurttila[5], Anna-Lena Fischer[2], Giacomo Salvadori[7], Andrea Cellini[1], Piotr Maj[1], Atsarina Larasati Anindya[1], Elin Claesson[1], Fangjia Luo[8,9], Tek Narsingh Malla[10,11], Suraj Pandey[10], Takehiko Tosha[8], Nuemket Nipawan[8,9,12], Shigeki Owada[8,13], Kensuke Tono[8,13], Rie Tanaka[8,9], Emina A. Stojković[14], Dmitry Mozorov[15], Pasi Myllyperkiö[15], Tatu Kumpulainen[15], Heikki Takala[5], Marius Schmidt[10], Janne A. Ihalainen[5], Sebastian Westenhoff[16]*

In photoactive proteins, coupling between the chromophore and protein matrix is exquisitely tuned. Proton transfer reactions can mediate this coupling, as in proton-coupled electron transfer and excited-state proton transfer. Additional mechanisms involving proton dislocations may exist but remain undiscovered. Here, we present a femtosecond crystallographic movie of the phytochrome from *Deinococcus radiodurans*. The structures reveal a space-conserving mechanism for rotation of the D-ring in the excited state. We observe rearrangement of a conserved hydrogen bond network within 300 fs, which precedes the isomerization reaction of the chromophore. Aided by molecular modeling and independently confirmed by femtosecond infrared spectroscopy, we attribute these changes to a protonation shift of the strictly conserved histidine-260. Although this histidine lies close to the photoexcited π-orbitals of the chromophore, it is not directly part of them. We propose that this "remote-controlled" proton transfer relays photoexcitation near-instantaneously to the protein matrix. This mechanism may be widely used to transduce cofactor signals to their hosting enzymes.

INTRODUCTION

Photoactive proteins are indispensable for supporting life on earth, both as photosynthetic entities that produce green energy and as photosensors that enable organisms to respond to light stimuli. For light activity, these proteins contain chromophore cofactors, which are coupled to the protein matrix at various levels. The protein binding pockets have specific electrostatics, polarities, and geometries, thus tuning the chromophores' electronic properties for optimal function (*1*). Photoexcited chromophores couple with the matrix through structural changes (*2*–*6*), and, reversely, ultrafast protein dynamics may influence chromophore photoreactions dynamically (*7*, *8*). Recent work on rhodopsin points to the fact that protein changes may precede structural changes in the chromophore, in particular with focus on changes in the hydrogen bond network (*5*, *9*–*12*). The chromophore-protein coupling is also critical for sustaining quantum coherences (*13*, *14*). Overall, it remains incompletely explored how chromophores interact with the protein matrix.

Proton transfer reactions play an important role in protein reactions, such as photosynthesis and respiration (*15*), and for fluorescent proteins (*16*). Typically, proton reactions serve to lower activation barriers and to impart directionality on enzymatic reactions. In the two established mechanisms, which are proton-coupled electron transfer and excited-state proton transfer, the initiating transfer originates on the electronically excited chromophore (*17*–*19*), which may subsequently dislocate protons along transfer chains that reach several residues away from the chromophores (*20*, *21*). Distinct from these two mechanisms, it is also plausible that ultrafast protonation changes occur close to the site of photoexcitation, but not directly on it (*12*). This may result in changes of H-bonding networks and would present a distinct coupling scheme between the chromophore and protein matrix.

We focus on phytochrome proteins, which sense red and far-red light in plants, fungi, and bacteria, providing light input to a variety of functions (*22*, *23*), and which are highly interesting for applications in optogenetics and agriculture (*24*). Phytochromes are homodimers, composed of highly conserved photosensory modules and varying output modules. The photosensory core consists of PAS (Per/Arnt/Sim), GAF (guanosine 3′,5′-monophosphate phosphodiesterase/adenylyl cyclase/FhlA), and PHY (phytochrome-specific) domains (Fig. 1A), which contain a bilin chromophore (Fig. 1B). Phytochromes interconvert between two photochemical states (Pr, λ_{max} = 650 to 700 nm; Pfr,

[1]Department of Chemistry and Molecular Biology, University of Gothenburg, 40530 Gothenburg, Sweden. [2]Department of Chemistry - BMC, Biochemistry, Uppsala University, 75123 Uppsala, Sweden. [3]Laboratory for Structural Dynamics of Receptors, Max Planck Society-Dioscuri Center for Scientific Excellence, Faculty of Biophysics, Biochemistry and Biotechnology, Jagiellonian University, Gronostajowa 7, 30-387 Krakow, Poland. [4]Department of Chemistry and Molecular Biology and the Swedish NMR Centre, University of Gothenburg, 40530 Gothenburg, Sweden. [5]Nanoscience Center, Department of Biological and Environmental Science, University of Jyväskylä, 40014 Jyväskylä, Finland. [6]Department of Chemistry, University of Washington, 109 Bagley Hall, Box 351700, Seattle, WA 98195-1700, USA. [7]Institute for Computational Biomedicine (INM-9), Forschungszentrum Jülich, 52428 Jülich, Germany. [8]RIKEN SPring-8 Center, Sayo, Hyogo, Japan. [9]Department of Cell Biology, Graduate School of Medicine, Kyoto University, Yoshidakonoe-cho, Sakyo-ku, Kyoto, Japan. [10]Physics Department, University of Wisconsin-Milwaukee, 3135 North Maryland Avenue, Milwaukee, WI 53211, USA. [11]Vaccine Research Center Electron Microscopy Unit, Frederick National Laboratory for Cancer Research, 8560 Progress Drive, Frederick, MD 21701, USA. [12]Chulabhorn International College of Medicine, Thammasat University, 99 Moo 18 Klong Luang, Rangsit, Pathumthani 12120, Thailand. [13]Japan Synchrotron Radiation Research Institute (JASRI), SPring-8, 1-1-1, Kouto, Sayo, Hyogo 679-5198, Japan. [14]Department of Biology, Northeastern Illinois University, 5500 North St. Louis Avenue, Chicago, IL 60625, USA. [15]Nanoscience Center, Department of Chemistry, University of Jyväskylä, 40014 Jyväskylä, Finland. [16]Science for Life Laboratory and Center for Chemical Mechanisms of Life, Department of Chemistry - BMC, Biochemistry, Uppsala University, 75123 Uppsala, Sweden.
*Corresponding author. Email: sebastian.westenhoff@kemi.uu.se
†These authors contributed equally to this work.

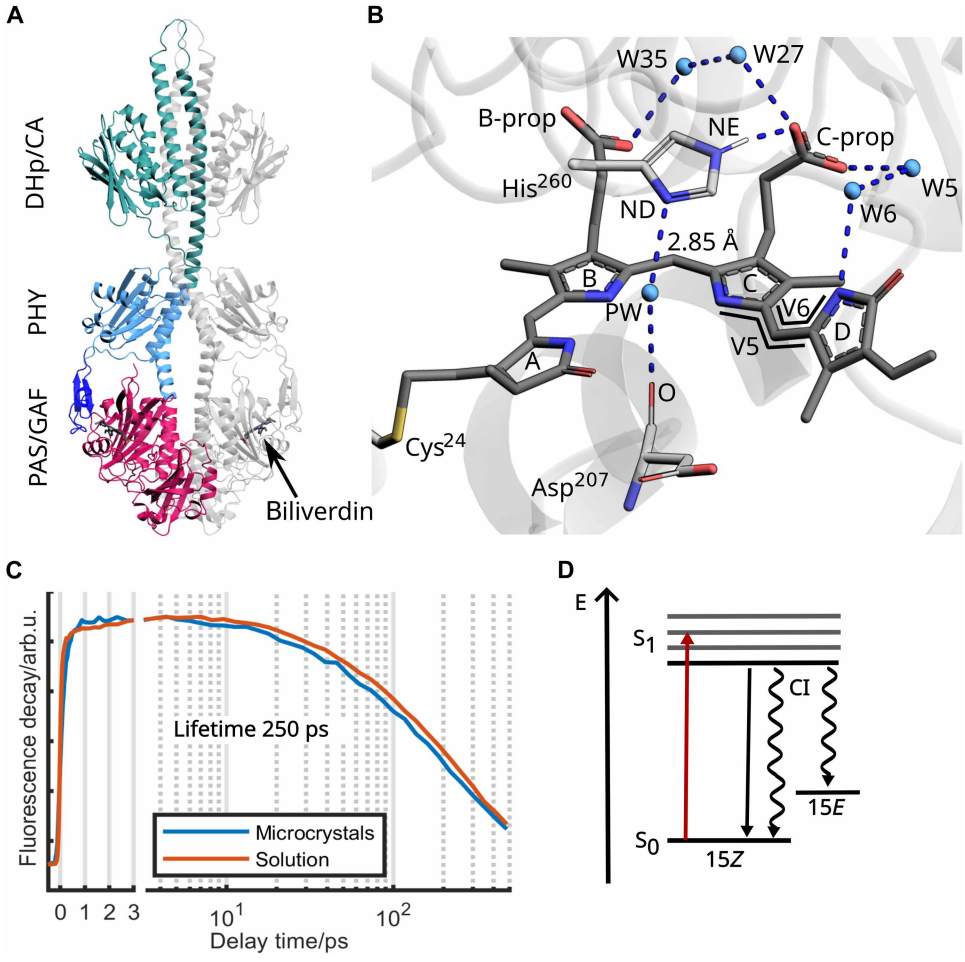

Fig. 1. Structure and primary photoreaction of *Dr*BphP. (**A**) Depicts an Alphafold prediction of the full-length *Dr*BphP structure (cartoon) with the PAS-GAF (pink), PHY (light blue), dimerization and histidine phosphor-transfer (DHp) and catalytic adenosine 5′-triphosphate binding (CA) domains (turquoise), and with the PHY tongue (dark blue) and biliverdin (BV, gray) marked. (**B**) The biliverdin chromophore (gray), selected amino acids (white), and water molecules (light blue spheres) of the refined dark structure of *Dr*BphP$_{PASGAF}$ are shown together with the hydrogen bond network, which wraps around the chromophore. V5 and V6 denote dihedral angles. (**C**) Fluorescence decay integrated over the entire spectrum of *Dr*BphP$_{PASGAF}$ as microcrystals and in solution. (**D**) An energy (E) diagram of the ground (S_0) and electronically excited Pr states (S_1). Deactivation is via a conical intersection (CI) to the resting (15*Z*) and Lumi-R (15*E*) conformations of the biliverdin (*38*). arb.u., arbitrary unit.

λ_{max} = 700 to 760 nm), with isomerization of the chromophore (Pr,15*Z*; Pfr,15*E*) and refolding of the so-called PHY tongue as characteristic features of this transition (*25*–*29*).

The primary photoreaction from Pr has been studied by ultrafast spectroscopy (*30*–*39*). As a minimal consensus, the electronically excited Pr state relaxes on the excited state surface by rotation of the D-ring (*35*, *40*), from where it converts back into the ground state via a conical intersection, thereby forming either the product state with isomerized D-ring in a 15*E* conformation (Lumi-R, yield of 10 to 15% in red/far-red phytochromes) or returning to the Pr ground state (Fig. 1D). Multiple spectroscopic studies provide evidence that isomerization of the chromophore in Pr occurs within tens to hundreds of picoseconds (*34*, *35*, *37*, *40*), even though recent theory has not been able to reproduce the long isomerization times (*41*, *42*). Heterogeneity in the chromophore conformation or the protein environment (*37*–*39*) and a picosecond structural response in the protein environment of yet unknown structural origin has been implicated spectroscopically (*36*). Despite this body of work, the structural evolution of the excited states is not clear.

To resolve femtosecond structural dynamics in the chromophore and protein, we use time-resolved serial crystallography (SX) at an x-ray free electron laser source (XFEL). This method has provided unique insight into the structural dynamics of proteins (*2*–*6*, *43*). Using time-resolved SX, we have previously reported structural changes at 1 and 10 ps after photoactivation of the PAS-GAF phytochrome fragment from *Deinococcus radiodurans* (*Dr*BphP$_{PASGAF}$) (*6*). In the *Dr*BphP$_{PASGAF}$ crystals, formation of the Lumi-R intermediate is muted; however, the excited state is similar to solution-state proteins (Fig. 1C). Here, we now report a full, time-resolved trajectory from 0 to 3 ps, identifying the structural mode of rotation of the D-ring and describing a previously unknown type of proton-coupled reaction mechanism.

RESULTS

High-quality difference electron density trajectories up to 3 ps were recorded from microcrystals of *Dr*BphP$_{PASGAF}$

Prior to the measurements at the XFEL, we characterized solution and crystal samples using time-resolved fluorescence spectroscopy

(Fig. 1C). We observe a small rise of the signal within the first picosecond in both samples, which indicates a relaxation process of or around the chromophore. Moreover, the fluorescence lifetimes of about 250 ps indicate that excited state decay occurs on the same time scale, in agreement with previous spectroscopic work (*34*, *35*, *37*, *40*, *44*).

We then recorded time-resolved SX data of microcrystals of *Dr*BphP$_{PASGAF}$ dispersed in grease at the SPring-8 Angstrom Compact Free Electron Laser (SACLA) BL3 beamline (tables S1 and S2) spanning delay times between −100 fs and 3 ps (fig. S1). The images were indexed, scaled, and averaged into 19 time bins (table S2) to produce difference structure factors $|\Delta F_{obs}|\ (t) = w\ (|F_{obs,\ light}|\ (t) - |F_{obs,\ dark}|)$, which were weighted with factor w to reduce the effect of outliers (see Materials and Methods), and Fourier-transformed into observed difference electron density (DED) maps with phases of the dark model (Fig. 2). Affirming the data integrity, the DED peaks are located around the chromophore region (fig. S2). The signals at a delay time of 720 fs (this study) overlap well with those at 1-ps delay time (previous work) (fig. S3) (*6*). The DED signals are similar but not identical between subunits A and B, as previously observed (*6*, *45*, *46*).

As in many time-resolved SX studies, high excitation fluences were used (3.9 mJ/mm^2 at an excitation wavelength of 640 nm). This raises the concern that multiphoton absorption influences structural dynamics (*47*). The excitation process in the partially opaque grease jets is a complex function of crystal position, crystal orientation, and various other effects, which may reduce the excitation intensity at the sample position (see Discussion). To experimentally

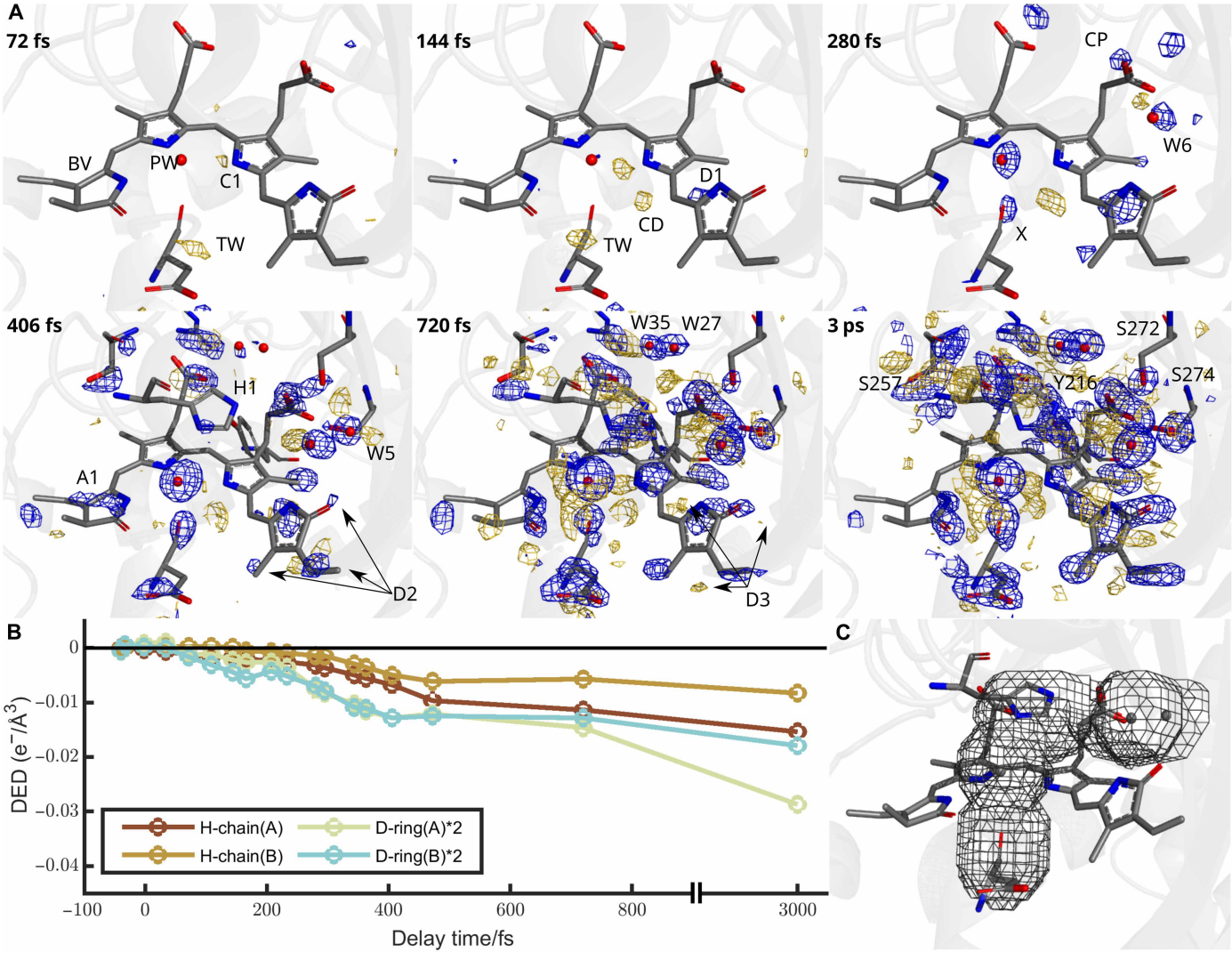

Fig. 2. DED features around BV (chain A) as a function of delay time and key structural changes of the chromophore and binding pocket from 0 to 3 ps. (**A**) The DED maps are shown around BV of the refined dark structure (residues and BV in gray sticks, water molecules as red spheres). The gold and blue DED features represent the positive and negative densities, respectively, and are contoured at 0.033 e$^-$/Å^3 for all time points. This corresponds to a root mean square deviation of close to 4σ for the maps. DED features marked are TW (transient water), C1 (close to C-ring), CD (C-D bridge), D1 (close to N atom of the D-ring), X (Asp^{207}), PW (pyrrole water), CP (C-propionate), A1 (A-ring), H1 (His^{260}), D2 (ethyl, methyl, and carboxyl group of the D-ring), D3 (close to D-ring), water molecules, and residues as indicated. (**B**) Integrated negative densities as a function of time around the D-ring of the biliverdin chromophore and around the hydrogen bonding chain region stretching from Asp^{207} over PW, His^{260}, C-prop, and waters to the D-ring NH. (**C**) The mask around hydrogen bonding chain for integration of the signal in (B) is shown.

verify that the DED maps are not dominated by effects of multiphoton excitation, we recorded DED maps at reduced laser fluences of 0.8 mJ/mm^2 (20% of the highest fluence) and 0.34 mJ/mm^2 (8.5% of the highest fluence) around 720 fs (table S1 and fig. S4). The amplitude of signals increases with excitation fluence, with some saturation observable for the highest fluence (fig. S4B). However, visual comparison of the shape of the DED signals (fig. S4) and high correlation coefficients in important regions of interest reveal that the shape of the DED signals is qualitatively similar for all three excitation fluences (fig. S5). Moreover, structures refined against the data from all three excitation fluences yield highly similar light-induced movement of the pyrrole water (fig. S6). This indicates that the structural findings described here are not the consequence of absorption of multiple photons.

Rotation of the D-ring is through a counterclockwise, space-conserving mechanism in agreement with recent quantum-chemical predictions

To analyze the complex signal patterns in the time-dependent DED maps [Fig. 2 and figs. S7 to S9 and S24; for a description of the short-lived DED feature TW (transient water), see figs. S10 and S11], we first focus on the DED signals around the D-ring of the biliverdin chromophore (Fig. 2A). The signals are found next to the D-ring (feature D1, negative, from 144 fs), at the three side groups of the ring (D2, negative, 406 fs), close to the NH group and behind the ring (D3, positive, 720 fs), and close to the bridge between the C- and D-rings (CD, positive, from 144 fs). These signals arise within 720 fs in both subunits (Fig. 2B). We also observe weaker DED signals on the A-ring (A1, negative, 406 fs). In line with expectations (*6*, *31*, *45*), these data indicate a notable rotation of the D-ring, whereas the A-ring undergoes displacement but not a rotation.

To further analyze these time-dependent DED changes, we refined structures against extrapolated structure factors. Here, an important parameter is the photoactivation yield, which is the proportion of atoms/molecules in the crystal that are photoexcited and undergo a structural change. We estimated the yield to 16.6% by tracking the appearance of negative densities in the extrapolated maps (see fig. S12) and assumed it to be the same for all time points. The agreement between calculated and observed DED maps is excellent in the entire chromophore binding pocket (fig. S14).

The refined time-resolved structures reveal that the rotation of the D-ring occurs in two phases (Fig. 3). The first phase culminates at a peak amplitude of ~25° (22° in subunit B) by 400 fs, and, in the second phase, the D-ring relaxes back to 10° at 3 ps (Fig. 3, A and D). The dihedral angles V5 and V6 at the bridge between C- and D-rings (Fig. 1B for definitions) initially change in opposing directions until they reach the inflection point at 400 fs (Fig. 3C and fig. S15). From here, both angles rotate inversely, whereby V5 overshoots, leading to a shifted and rotated D-ring configuration at 720 fs and at 3 ps.

Notably, the first phase of the movements of the D-ring agree very well with two recent quantum mechanics/molecular mechanics (QM/MM) simulation studies of the excited state dynamics in *Dr*BphP, which both predicted counterclockwise rotation of the D-ring in the biliverdin excited state with an initial change of V5 and V6 in opposing directions (*41*, *42*). Figure 3E shows the simulated evolution of the angles, extracted from the part of the QM/MM trajectories that were in the excited state (see figs. S25 and S26) by Morozov *et al.* (*42*). Agreement with the experiment is observed for time and angular changes prior to reaching the conical intersection (compare Fig. 3, D and E). Thus, both experiment and theory show that the biliverdin in bacterial phytochromes approaches the conical intersection in a space-conserving and counterclockwise rotation of the D-ring.

While productive isomerization should proceed by rotation into higher V6 angles, our refined structures show that the chromophore structure relaxes back into a less twisted geometry at 3 ps. Considering our observation of the long-lived fluorescence in the crystals (Fig. 1C), we consider that this is the structure of a relaxed excited state (*37*).

Concerted changes in the hydrogen bond network around the chromophore are driven by an ultrafast protonation change of histidine-260

Next, we turn our attention to DED changes along the conserved hydrogen bonding network (Figs. 1B and 2). We observe strong positive and negative DED features at the C-ring propionate (feature CP in Fig. 2), waters 5 (W5) and 6 (W6) connecting to the D-ring, around the pyrrole water (feature PW), on Asp^{207} (feature X), and close to His^{260} (H1). The signal also spreads via waters 27 (W27) and 35 (W35) to the propionate group of the B-ring. These signals build up within 400 fs and are sustained until the last time point at 3 ps (Fig. 2), with the signals at 720 fs and 3 ps matching previous observations at 1 and 10 ps (*6*). We consider these DED signals to predominantly arise from structural changes in the first excited state, because of the high correlation of signals of the DED maps between high and low excitation fluences (figs. S4 and S5) and because the D-ring trajectory up to 400 fs agrees well with theory (see above).

From the refined structures, we find that the distance between PW and its H-bonding partner His^{260} increases rapidly. Assuming a cutoff at 3.3 Å, the hydrogen bond breaks at ~300 fs (Fig. 4B). This movement is accompanied by rotation of the His^{260} side chain by 25° within 400 fs (Fig. 4B). Moreover, the bond distances of the PW to its remaining H-bonding partners (Asp^{207} and the NH groups of the A-, B-, and C-rings of BV) also increase (fig. S16). These movements are intriguing, because the moieties are not part of the π-conjugated system of the biliverdin, yet they occur within 300 fs before a signal could have been transduced by steric effects. Thus, an unknown chemical mechanism must be at play, which couples the electronic excitation of the chromophore to the protein binding pocket.

As potential mechanisms, we consider photoexcitation of BV, which leads to charge reorganization in the molecule and could displace the PW by coulomb forces (*5*, *12*), and proton or charge transfer reactions involving the His^{260} side chain. The SX data do not resolve the electron densities of protons or electrons directly; however, as the protonation and charge state of His^{260} and BV are expected to sensitively control the position of water molecules in the binding pocket (*48*), the DED signals of the waters can be used as a probe. To test these scenarios, we predicted electron density maps of the waters from heavy atom restrained molecular dynamics (MD) simulations in several different protonation and photoexcitation configurations and compared those to the experiment (fig. S17).

We first generated MD trajectories based on structures of the dark state with His^{260} in different protonation states. This confirmed that His^{260} is protonated at the epsilon nitrogen in the dark (termed HIE) (*49*), as only this configuration reproduced the water positions of the dark crystallographic data satisfactorily (fig. S18). Then, we

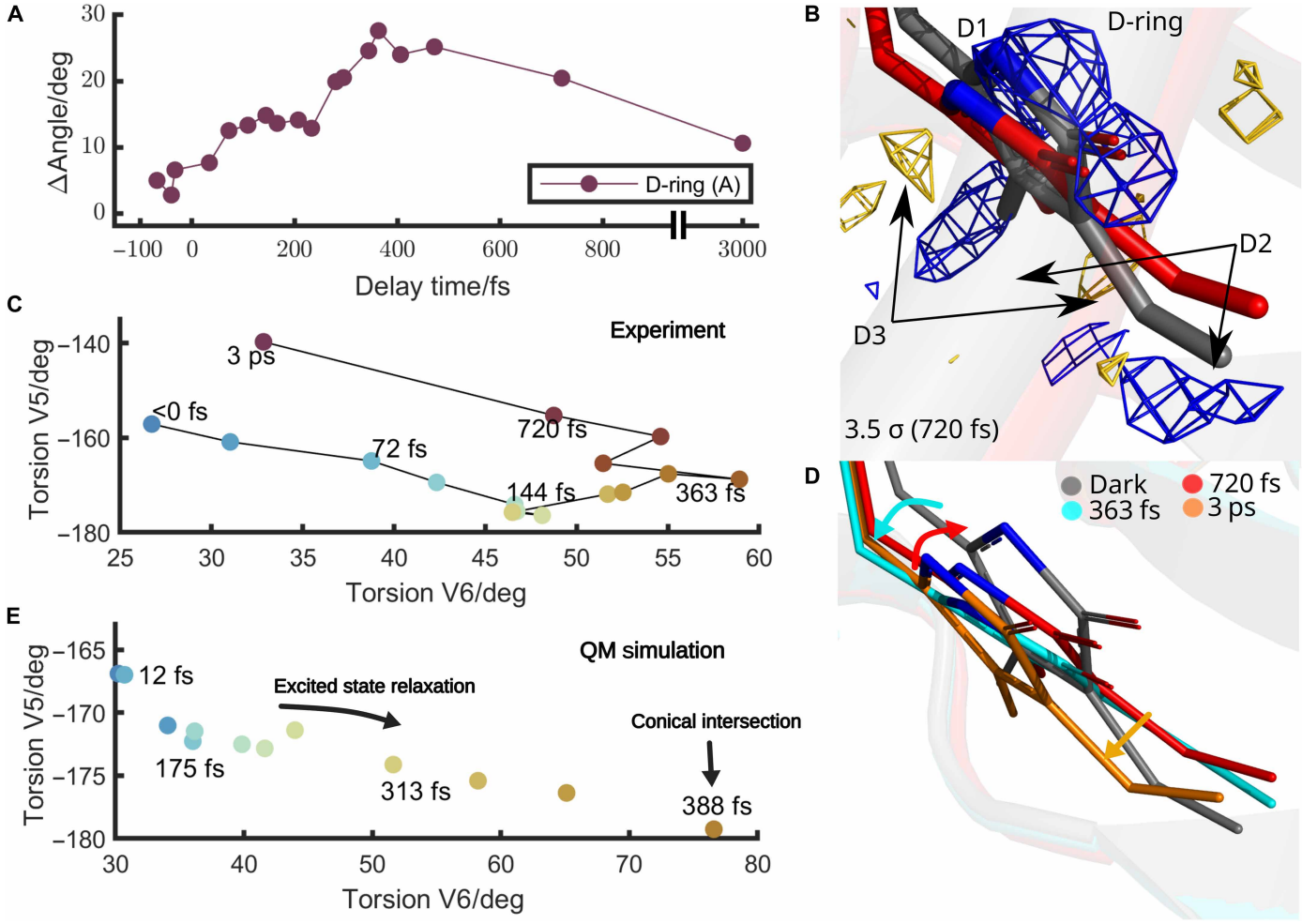

Fig. 3. Structural analysis of changes around the D-ring demonstrates space-conserving, counterclockwise rotation in the first excited state. (**A**) The change of angle of the plane of the D-ring referenced to dark structure is shown as a function of time. (**B**) Observed DED map [positive DED (gold mesh) and negative DED (blue mesh) around the D-ring of dark (gray sticks) and 720 fs (red sticks) structure]. The positive DED features (D3) and the negative DED features (D1 and D2) are marked with arrows. (**C**) Torsion angles V5 and V6 of the refined structures, plotted for time points (in femtoseconds): −68, 34, 72, 109, 144, 166, 207, 233, 280, 295, 344, 363, 406, 472, 720, and 3000. (**D**) Structural overlay of the D-ring in refined structures as indicated in the panel legend. The arrows indicate the main movement and are color-coded according to the target time point: a twist from dark to 363 fs (cyan), the inversion of the twist from 363 fs to 720 fs (red), and further inverted twist and displacement from 720 fs to 3 ps (orange). (**E**) Evolution of the same angles as in (C) extracted from all trajectories in (*42*). The trajectories were aligned in time to the point of state flip to the ground state, which was defined to be at 400 fs, and binned into the time bins with centers at 12, 75, 125, 175, 212, 238, 262, 288, 313, 338, 362, and 388 fs. All trajectory data plotted in the panel are from trajectories in the S_1 excited state (see fig. S25).

computed trajectories with the biliverdin simulated in the excited states. To do so, the GAFF force field (*50*) of biliverdin was refined against point charges obtained from time-dependent density functional theory (TD-DFT) computations of the excited state, with the structure of biliverdin (see Materials and Methods). Using the structure of the protein at 3 ps, we tested protonation at the delta nitrogen (HID*), the epsilon nitrogen (HIE*), double protonation at both nitrogen atoms (HIP*), and additional models of HIP + PW as OH^- and a radical $His^{260}\cdot$ + $BV^{-}\cdot$ ($His^{260}\cdot$ deprotonated and $BV^{-}\cdot$ protonated at the C-propionate). By subtracting the simulated maps of HIE (dark) from the various maps of the BV in the excited state (marked by *), we generated simulated DED maps (Fig. 4C and figs. S19 to S22).

This analysis revealed that configurations where the delta nitrogen of His^{260} is protonated in the excited state (HID*-HIE and HIP*-HIE) give notably better agreement with experimental DED [Pearson correlation coefficient (PCC) > 0.80] compared to the HIE*-HIE (PCC < 0.58) and the two additional setups (PCC < 0.7) (Fig. 4C and fig. S22). As internal control, we repeated the simulations three times. We also verified that the PCCs are similar for all tested configurations in the region around W5 and W6, where we do not expect strong sensitivity to the protonation state of His^{260} (fig. S19).

This analysis suggests that the electric dipole changes on the BV due to photoexcitation alone (represented by the candidate model HIE*-HIE) is insufficient to displace the PW. This finding is consistent with literature, as QM/MM simulations of the photoactivation process, which allowed for partial charge transfer in the excited state, but not proton transfer, did not show notable movement of PW after photoexcitation (fig. S23) (*41*, *42*). Instead, good agreement with the experiment is only obtained for cases where His^{260}

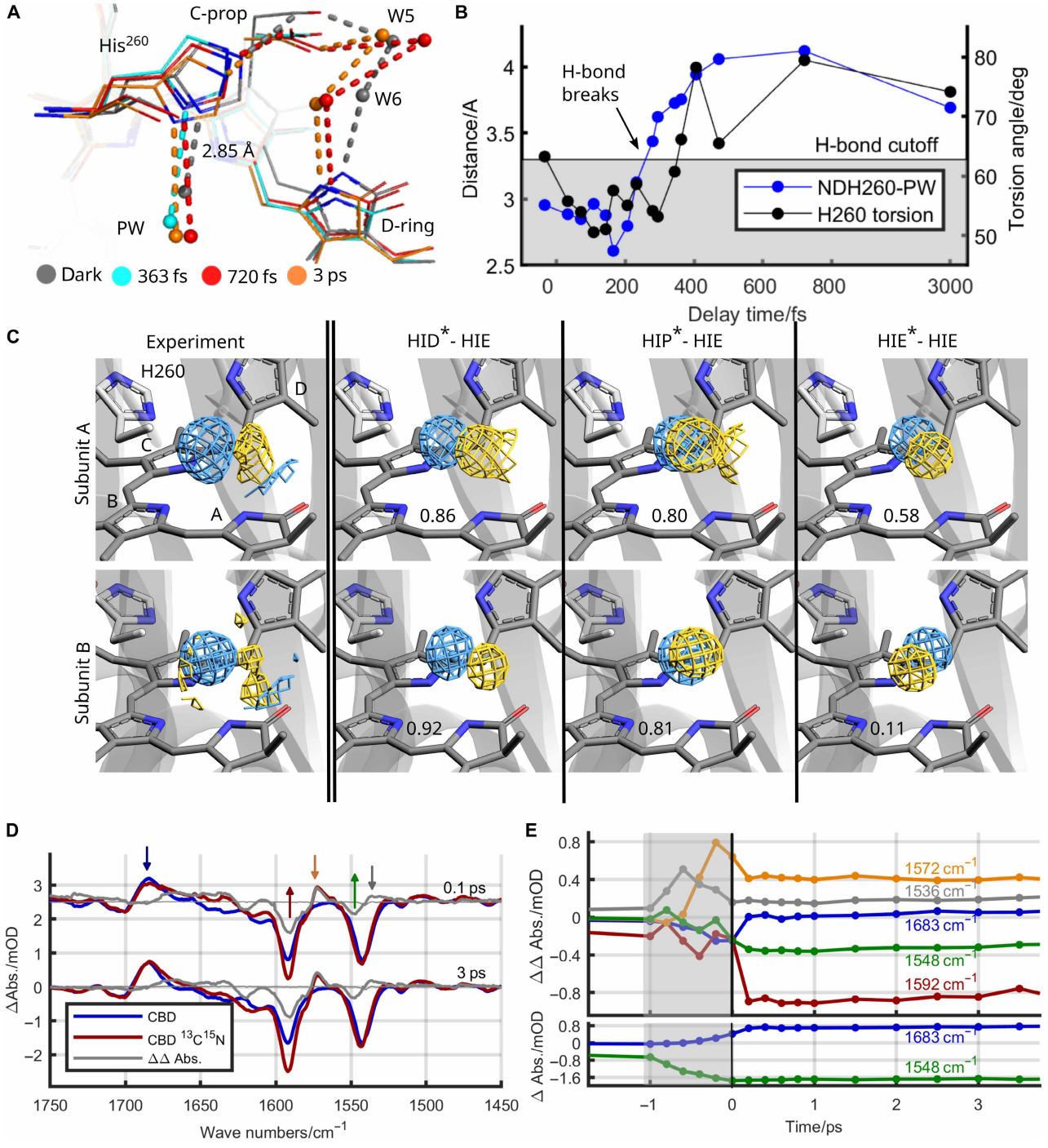

Fig. 4. Changes in the H-bonding network are caused by ultrafast protonation changes of His^{260}. (**A**) Structure view of refined water positions. The distance between the delta nitrogen of His^{260} and PW in the dark structure is shown. (**B**) Distance and angular analysis show that the hydrogen bond between His^{260} and PW breaks within 300 fs (cutoff of 3.3 Å) and that this coincides with rotation of the His^{260} side chain. (**C**) The experimental DED at 3 ps is compared to difference water density maps calculated from three MD setups (see Materials and Methods) in subunits A and B (top and bottom row). BV and His^{260} from the refined dark structure are shown in gray sticks and PW as blue spheres. The light blue and gold contours illustrate negative and positive densities, respectively, and the Pearson correlation coefficient (PCC) between the experimental DED and the calculated difference water density map around the PW is stated (see Materials and Methods). (**D**) Time-resolved IR spectra of *Dr*BphP$_{PASGAF}$ (CBD) and *Dr*BphP$_{PASGAF}$ labeled with $^{13}C^{15}N$ (chromophore nonlabeled), averaged over time points 0 and 0.2 ps (marked as 0.1 ps), and over 2.5 and 3.5 ps (marked as 3 ps). The difference between the labeled and nonlabeled signal is the double-difference absorption (ΔΔAbs, gray). The signal at 1683 cm^{-1} (blue) originates from the photoinduced absorption of the biliverdin carbonyl vibration (*51*) and was used to scale the intensities of the nonlabeled and labeled *Dr*BphP$_{PASGAF}$ data. The arrows indicate the spectral positions for kinetic analysis. (**E**) Kinetic traces of ΔΔAbs at selected wave numbers (top) and of ΔAbs (bottom) reveal that the changes in the protein scaffold arises directly after photoexcitation. The dataset shows pronounced perturbed free induction decays prior to 0-time (gray-shaded area), which does not carry interpretable information (*101*). The estimated time resolution is 200 fs.

changes protonation state after photoexcitation of the biliverdin (as in HID*-HIE and HIP*-HIE). The protonation delivers a strong enough disruption to the hydrogen bonding network to explain the observed changes. The time-resolved crystallographic data indicate that this change occurs within <300 fs (Fig. 4B).

Femtosecond time-resolved infrared spectroscopy indicates an ultrafast chemical change in protein matrix, with spectral positions matching histidine absorptions

To corroborate these findings, we recorded femtosecond infrared (IR) spectra of *Dr*BphP$_{PASGAF}$ in solution. In one of the two samples, the protein, but not the chromophore, was labeled with $^{13}C^{15}N$. This shifts all protein peaks by tens of wave numbers, and, consequently, spectral differences between the labeled and unlabeled samples indicate protein contributions. The double-difference absorption spectra (ΔΔAbs; Fig. 4D) show distinct differences at 1592 (−)/1572 (+) cm^{-1} and 1548 (−)/1531 (+) cm^{-1} at 0.1 and 3 ps delay times. This four-peak pattern is characteristic for an isotope-induced shift on a difference IR spectrum. The kinetics of the double differences reveal that the protein-associated signals arise immediately after photoexcitation, in concert with photoexcitation of the chromophore, which is observable in the single-difference spectra as the positive biliverdin carbonyl signal at 1683 (+) cm^{-1} (Fig. 4E) (*51*). This demonstrates that the protein scaffold undergoes a chemical change on ultrafast time scales prior to the primary photoreaction of the biliverdin chromophore. Even though we cannot assign the peaks definitely to a specific residue based on the present data, we note that characteristic IR peaks of the histidine tautomers HID and HIE are expected in the region 1560 to 1610 cm^{-1} (*52*), matching the recorded double-difference spectra (Fig. 4D). We remark that we do not observe any strong chromophore-associated peaks in the 1700 to 1750 cm^{-1} spectral region, which excludes protonation of the propionate side chain as the driver for the observed changes. Thus, the IR spectra are in agreement with ultrafast protonation of the delta nitrogen of His^{260}.

DISCUSSION

Here, we report the structural evolution of the photoexcited state of biliverdin in a phytochrome in the Pr state. Time-resolved SX data do not directly reveal if the observed changes are in the electronically excited or ground states. However, the long-lived fluorescence decay (Fig. 1C) does not decay within the first picoseconds, which indicates that the crystallographic snapshots up to 3 ps are from the excited state, prior to deactivation of the chromophore to the ground state. Consequently, isomerization of the chromophore is not observed in the presented SX data. The structural evolution within the first 400 fs reveals that V5 and V6 counter-rotate so that the D-ring can twist in a space-conserving way in the excited state, which agrees with QM/MM predictions (*41*, *42*). In the experiments, maximum rotation is reached at ~400 fs (25° in subunit A and 22° in subunit B), from where the angles relax again, with the D-ring assuming a shifted position. We assign this to be the structure of the fluorescent excited state.

Concerns have been raised regarding the high pump fluence that is used in time-resolved SX studies (*47*, *53*). In this study, several considerations support that the conclusions drawn in this paper are not due to multiphoton absorption. First, our power dependence analysis demonstrates that the pyrrole water and D-ring signals are invariant over a large range of pump powers (fig. S4A). Structural fits indicate that the movement of the pyrrole water is similar between highest and lowest fluence (fig. S6). Thus, it appears that the laser intensity absorbed by the chromophore is lower than predicted. This could be explained by scattering of the pump light in the grease-microcrystal mixtures (*6*), multiphoton absorption in the grease matrix (*54*), and noncollinear alignment of the chromophores with laser polarization (*55*). Moreover, the DED signal around the chromophore rises much slower and persists much longer than the decay time of higher lying states, which would be excited if multiphoton absorption was active (*53*). Last, our IR spectroscopic data (Fig. 4) independently confirm the process with much lower pump fluences under the multiphoton threshold. These considerations indicate that the observed structural changes are part of the linear response of the chromophore to photoexcitation.

The time-resolved structures of the phytochrome reveal that photoexcitation of the chromophore leads to an ultrafast protonation event, which occurs remotely from the chromophore (Fig. 5) (*12*). We term this change as remote, because it does not occur directly on the photoexcited, π-conjugated orbitals of the chromophore. As such, the mechanism is distinguished from proton-coupled electron transfer or excited state proton transfer (*17*–*19*), where the photoexcited portion of the chromophore would be directly involved in the transfer event.

The proposed change in protonation requires a residue with a pK_a near physiological pH, such as histidine, whose protonation state can be influenced by its environment. Transient alteration of

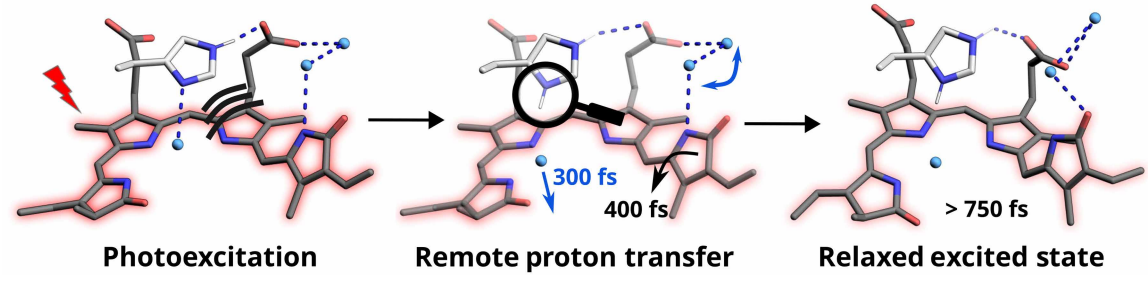

Fig. 5. Scheme of remote-controlled proton transfer and rotation of D-ring. Photoexcitation of the biliverdin chromophore (in sticks) leads to an ultrafast change of protonation at His^{260} (left side: with epsilon hydrogen bond; middle and right side: with both epsilon and delta position with hydrogen atoms), which is not part of the photoexcited π-system. This change in configuration is the driving force behind the movement of the key pyrrole water molecule in the binding pocket and occurs within 300 fs, while the rotation of the D-ring takes 400 fs. The right side shows the relaxed excited state structure, which is observed after 750 fs.

the pK_a of histidine by the photoexcitation of the chromophore is conceivable, potentially caused by redistribution of charge density (Fig. 5), similar to the "coulomb hammer" mechanism (*56*). Similar couplings have been inferred spectroscopically on ultrafast time scales in proteins (*9*, *57*), have been shown to have conformational effects in model systems (*58*), and have been proposed to play a role in phytochromes (*19*, *32*, *59*).

It is interesting to consider the source of the proton. Realistic candidates are abstraction from the pyrrole water, donation by the chromophore, a rotational motion of the side chain of His^{260}, and a tautomerization reaction of His^{260}. Given the lack of agreement between our simulation of HIP + PW (OH^-) with the experiment (fig. S22), and because of the observed peak shift in the IR spectra that matches corresponding histidine absorptions (Fig. 4D), we do not think that abstraction from pyrrole water is likely. A 180° rotation of the His^{260} side chain is a possible explanation. Such rotation would not imply proton transfer per se, but effectively result in very similar consequence for the H-bonding network. However, since we do not observe such a motion in the time-resolved DED maps, we tentatively rule this mechanism out. A third possibility is that the chromophore itself acts as a proton donor. Excited state proton transfer has been implicated for bilins in phytochromes (*19*, *44*) and in solution (*60*), but the mechanism remains controversial. Last, a tautomerization reaction of the histidine side chain, possibly linked to the hydrogen bonding chain surrounding the chromophore, could lead to fast protonation changes. This is our preferred possibility and could act together with other sources, i.e., chromophore deprotonation. We note that further research is required to conclusively distinguish between these possibilities.

We conclude that His^{260} of *Dr*BphP$_{PASGAF}$ plays a key role in the photoexcitation dynamics of phytochromes. His^{260} is strictly conserved in the phytochrome superfamily, buffers the biliverdin in the ground state (*61*), and is heterogeneously protonated in a cyanobacteriochrome (*48*). His^{260} mutants lose their ability to photoconvert to Pfr, with the exception of mutation into dibasic glutamine, which may retain some ability for the proton transfer reaction (*62*, *63*). These previous findings are consistent with the proposed ultrafast reaction of His^{260}.

The ultrafast nature and directionality of rearrangement of the hydrogen bonding network is intriguing. The reaction (<300 fs) occurs in concert with the twisting motion of the D-ring and before the ring reaches the most twisted conformation (~400 fs; Fig. 5). Since the efficiency of isomerization is thought to depend on the connected hydrogen bond environment of the D-ring (*41*, *44*), it is conceivable that the observed changes dynamically control the activation energy leading to isomerization (Fig. 1D). This could effectively promote unidirectionality of the photoreaction. Moreover, on the opposing end of the hydrogen bonding chain, the functionally important Asp^{207}, which connects to the PHY tongue, is notably moved already at 200 fs (Fig. 2A and fig. S7). Even though the tongue region is truncated in our construct, it is reasonable to assume that these ultrafast changes modulate the stability of tongue region.

Last, we speculate that the observed changes may constitute a low-energy vibrational mode of the protein, which is activated by photoexcitation of the chromophore (*14*, *64*). These modes have only subtle effects on the electronic states and are mainly considered isotropic heat sinks. The remote proton response on the pyrrole water may challenge this view as the process appears highly directed. While our data are not conclusive as to how the process couples to the excited state, the fact that water movements occur on the same time scales as the D-ring rotation supports this possibility.

Here, we find remote-controlled protonation changes of His^{260} as a mean for anisotropic and ultrafast transduction of a photoactivation signal into the protein matrix of a phytochrome. The mechanism serves the general requirement of signaling proteins to develop long-range structural signals from light cues. We propose that it may be a widely used mechanism in natural systems and that it could be exploited in novel bioinspired, supramolecular chemistry applications.

MATERIALS AND METHODS

Protein purification and crystallization

The PAS-GAF fragment (amino acids 1 to 321) from *D. radiodurans* (*Dr*BphP$_{PASGAF}$) in vector pET21b (+) (*63*) was expressed and purified as previously described (*29*). Briefly, the recombinant protein was expressed in *Escherichia coli* strain BL21 (DE3) with Ho1 yielding holoprotein. Full biliverdin incorporation was achieved by adding 8 mg of biliverdin hydrochloride (Frontier Scientific) per liter of cell culture to the cell lysate and incubated overnight at 10°C. The protein was purified with HisTrap HP column (GE Healthcare) in 30 mM tris (pH 8), 50 mM NaCl, and 5 to 500 mM imidazole and followed by a HiLoad 26/600 Superdex 200 pg column (GE Healthcare) in buffer of 30 mM tris (pH 8). For the production of 13C15N isotopically labeled samples, a protocol described in was followed. (*65*) The proteins were concentrated to ~25 mg/ml and flash-frozen in liquid nitrogen.

Microcrystal preparation

All crystals were set up under green safe light and grown in the dark. Batch crystallization was performed as described (*6*). To summarize, 50 µl of concentrated protein (25 to 30 mg/ml) was added to 450 µl of reservoir solution (60 mM sodium acetate, pH 4.95; 3.3% polyethylene glycol, molecular weight 400; 1 mM dithiothreitol; and 30% 2-methyl-2,4-pentanediol) and immediately mixed. The batch microcrystal tubes were left on a tipping table at 4°C for 48 hours. The microcrystals were pelleted, and 400 µl of supernatant was removed. An additional 200 µl of protein (14 mg/ml) was added to the microcrystals along with 200 µl of fresh reservoir solution. The microcrystal tubes were left on the tipping table at room temperature for another 48 hours.

SX data collection

Serial femtosecond crystallography data were collected at the SACLA beamline BL3 in June 2021. The microcrystals were embedded into grease and delivered to the setup through a 100-µm nozzle (4.24 µl min^{-1}). The sample was illuminated at 15 Hz with optical laser pulses. These had a center wavelength of 644 nm and were focused into a spot of 163 µm by 173 µm ($1/e^2$). With a pulse energy of 10 µJ, 21 µJ, and 112 µJ, this yields a laser fluence of 0.34 mJ/mm^2, 0.8 mJ/mm^2, and 3.9 mJ/mm^2, respectively. As discussed previously, scattering of the jet surface and air bubbles in the grease lead to reduction of the effective photon flux by about an order of magnitude (*6*).

For most of the time-resolved experiments, we used the highest laser fluence and probed with the x-ray pulses delivered by SACLA (7 keV, 10 fs, 30 Hz), which were controlled to arrive at defined delays from −0.1 to 3 ps after the optical laser pulse. The timing tool was used to increase timing accuracy. The nominal time-resolution

of the setup at SACLA was 50 fs. We have considered the possibility that multiple scattering events of the optical laser could, in principle, reduce the time resolution of the experiment. For example, using a diffusion coefficient of $D = 0.07$ cm^2/ns (7.0×10^{-6} m^2/ns), representative of very strongly scattering media, and using the diffusion equation $\Delta t = L^2/6D$, we estimate a theoretical pulse broadening of ~60 fs at the center of the jet ($L = 50$ μm). The true broadening will be lower, because the direct beam will also hit the crystals and will be higher in intensity. We conclude that this level of broadening is unlikely to notably degrade the time resolution of the experiment. Due to this effect and velocity mismatch, we conservatively estimate an upper limit for the timing accuracy to be 150 fs. We observe a TW signal that arises and decays within 200 fs (fig. S11E), so the true time resolution is likely lower than this. Diffraction patterns were recorded using the phase 3 multi-port charge-coupled device detector (MPCCD) detector with eight modules (*66*). We verified that there was no residual photoexcitation from previous laser shots in the "dark" x-ray diffraction. In addition, a dark run with the optical laser blocked was recorded for calculating the dark structure without any chance of light contamination.

Processing of diffraction images

Diffraction images with Bragg spots from microcrystal diffraction were identified using peakfinder8 in Cheetah (*67*, *68*). These images were input to CrystFEL (version 0.9.1) (*69*) for indexing, using xgandalf with the settings: min-snr = 4.5, threshold = 100, minimum pixel counts = 2. The resulting indexed patterns were scaled and merged using the program partialator (–model = xsphere) in CrystFEL to yield the structure factor amplitudes ($|F_{obs}|$). The data quality statistics were calculated using the comparehkl and checkhkl programs available in CrystFEL (see tables S1 and S2).

Nominal delay times were corrected for jitter between x-ray and laser using the Arrival Timing Monitor at SACLA (*70*). The indexed patterns are binned according to their corrected delay time. Figure S1 shows the distribution of delay times for the recorded images.

Calculation of DED maps

The DED maps ($\Delta\rho$) are the Fourier transform of the observed difference structure factor amplitude ($|\Delta F_{obs}| = w\,(|F_{obs,\,light}| - |F_{obs,\,dark}|)$, with phase from the refined model in dark. w is a weighting factor calculated for each reflection (h, k, l) to reduce the effect of the outliers (*71*)

$$w = \left[1 + \frac{(\Delta Fo)^2}{\left\langle (\Delta Fo)^2 \right\rangle} + \frac{\left(\sigma_{\Delta Fo}\right)^2}{\left\langle \left(\sigma_{\Delta Fo}\right)^2 \right\rangle}\right]^{-1}$$

with σ as the standard deviation of the reflection. The Fourier transform was carried out using the program fft in the CCP4 suite (*72*). Before subtraction, $|F_{obs,\,dark}|$ and $|F_{obs,\,light}|$ were scaled using Scaleit, which is also available in the CCP4 package. In a first scaling step, $|F_{obs,\,dark}|$ was scaled to $|F_{calc,\,dark}|$, where F_{calc} values are the calculated structure factor amplitudes from the refined dark structure model, and then, $|F_{obs,\,light}|$ is scaled to $|F_{obs,\,dark}|$. This ensures that the DED maps are on an absolute unit of [e$^-$/Å^3].

Refinement of the dark structure

The dark structure was solved using the *Dr*BphP$_{PASGAF}$ crystal structure available in Protein Data Bank (PDB) with identification number 6T3L (*6*). The refined dark structure has an Rwork/Rfree of 0.023/0.019 and no Ramachandran outliers (tables S1 and S2). Molecular replacement and refinement were done using Phenix (*73*). Model building with step-to-step validation was performed using Coot 0.8.2 (*74*).

Extrapolated map calculation

To refine structures against the time-dependent structure factors, we used extrapolated structure factors ($|F_e|$), which were calculated as described previously (*6*, *75*). $|F_e|$ is calculated as $|F_e| = |F_{dark,\,c}| + N\,|\Delta F_{obs}|$. $|F_{dark,\,c}|$ denotes the calculated structure factors of the refined dark structure and N is the extrapolation factor, which is related to the photoexcitation yield $\alpha = (2/N)$. The factor 2 originates from the difference Fourier approximation (*76*). For computation of maps, the phases of the dark structure were used. N and correspondingly α were estimated using two methods: first, by analysis of the negative intensity in extrapolated maps computed as a function of N, and, second, by inspecting the agreement of computed and experimental DED features in the chromophore binding pocket (figs. S12 and S13).

Light activated structure refinement

The light structures were refined using Phenix (*73*) against the extrapolated structure factors $|F_e|$ and using dark phases. We used a fully automated refinement script CBD_refine.sh, which is available in the Supplementary Materials, and the same refinement parameters for all time points. The refinement was in reciprocal space and restricted to 10 Å (30 Å for 3 ps) around the PW of each subunit and using the dark structure as a starting model. Furthermore, the PCC (*6*, *45*) was used to validate the calculated DED maps from the refined light structure against the experimental DED map around the forementioned radius region. The agreement with the observed DEDs is excellent (fig. S12, D to F).

MD simulations: Structure preparation

The refined structure of *Dr*BphP$_{PASGAF}$ in the dark and the light state (3 ps) were used as initial atomic coordinates. MODELLER (*77*) was used to add the missing residues in the refined crystal structures (chain A: residues 130 to 136, chain B: residues 4 to 6 and 132 to 136). The H++ program (*78*) was used to determine the protonation state at pH 5.0 with further manual inspection afterward (table S3). The protonation state of His^{260} was not determined via H++, but was found to be protonated at the epsilon position (HIE) in the dark state by comparison of the dark state MD simulations (see below) to the experimental polder omit map of the dark state (fig. S18). The Pearson correlation between the crystallographic maps and simulations was computed using the masks depicted in fig. S21. The light state structures were protonated in four different ways: either at the epsilon position (HIE*), the delta position (HID*), both positions (HIP*), or not at all with a neutral charge (radical), which has been proposed before, forming a stable radical complex with the biliverdin (*79*). The AMBER ff14SB force field (*80*) was used for the protein, while the GAFF force field (*50*) was used for the biliverdin and for the bonding interactions between biliverdin and the covalently bonded Cys^{24}.

The biliverdin with an overall charge of −1 was protonated at all nitrogen atoms, and both propionate groups were deprotonated (*81*). The parameters for the biliverdin in the ground state were provided by Macaluso *et al.* (*82*). The biliverdin in the excited state was

parameterized by first optimizing the 3 ps BV structure in Gaussian 16 using TD-DFT, while the dihedrals between the A-, B-, C-, and D-ring together with the dihedrals of the B- and C-propionate were restrained. The optimization was done with the CAM-B3LYP/6-31+G (d,p) functional (*83*) in implicit water (*84*). The partial charges of the excited biliverdin were then calculated using the restrained electrostatic potential (RESP) protocol (*85*) in combination with an electrostatic potential calculation performed with TD-DFT and the CAM-B3LYP/6-31+G (d,p) functional in implicit water.

The calculation of the radical parameters is described below. Afterwards, tleap, implemented in AmberTools23 (*86*), was used to solvate the truncated dimers in a box of TIP3P (*87*) water molecules with a minimum wall distance of 10 Å to the protein. A uniform background plasma was used to neutralize the charges (*85*). The solvated structures were then restrained with a restraint weight of 1000 kcal mol^{-1} $Å^{-2}$, and only the water molecules were minimized and equilibrated using a multistep equilibration protocol (*88*, *89*).

MD simulations: Parameterization of the pyrrole water hydroxide and the radical pair His^{260}:BV^{-}

The parameters for the pyrrole water hydroxide with a charge of −1 were calculated using a standard RESP protocol (*90*) in combination with an electrostatic potential calculation performed with the HF/6-31G (d) method. The parameters for His^{260} and biliverdin in a radical state have been calculated separately, using the same protocol proposed by Macaluso *et al.* (*82*). First, the GAFF atom types (for biliverdin) and AMBER atom types (for His^{260}) were initially determined in antechamber (*50*) and then adjusted to accurately represent the conjugation pattern. His^{260} was deprotonated but remained neutral, while biliverdin was protonated at the C-propionate, still maintaining an overall charge of −1. Before calculating the partial charges, histidine was optimized using the B3LYP/6-31G* method with a multiplicity of 2 and biliverdin was optimized with TD-DFT and the CAM-B3LYP/6-31+G (d,p) functional in implicit water with a multiplicity of 2. The partial charges of the biliverdin and histidine were calculated separately using the RESP protocol (*90*) in combination with an electrostatic potential calculation performed with the HF/6-31G (d) method for the His^{260}, while TD-DFT and the CAM-B3LYP/6-31+G (d,p) functional in implicit water were used for the biliverdin.

MD simulations: Heavy atom restrained simulations

To elucidate the water rearrangement upon light activation around the biliverdin, heavy atom restrained MD simulations were performed in an NpT ensemble using the pmemd.cuda module of AMBER23 (*91*). A time step of 2 fs was used, and the lengths of all bonds involving hydrogen atoms were constrained using the SHAKE algorithm. The temperature was maintained constant at 300 K using the Langevin thermostat (*92*). For the pressure adjustment at 1 bar, the Berendsen barostat was used (*93*). To deal with long-range coulombic interactions, the particle mesh Ewald (*94*) was used with a real space cutoff of 8 Å. The structures were simulated for 3 × 100 ns using a restraint weight of 1000 kcal mol^{-1} $Å^{-2}$ on all protein heavy atoms.

MD simulations: Computation of DED maps

The obtained trajectories were aligned on the initial crystal structures, and each frame was converted into a water density map in the sfall program implemented in CCP4 using only water molecules around the chromophore region. The water density maps were calculated of each trajectory using P1 space-group, grid sampling along the *x*, *y*, and *z* axis was set to 120, 250, and 250, and the cell dimensions were the same as the refined crystal structures. The calculated water density maps were then averaged for each trajectory, and the averaged dark state water density map was subtracted from each light state trajectory. The resulting computed water difference maps were then used to directly compare them visually and quantitatively to the experimental DED maps (see Fig. 4C and figs. S19, S20, and S22). The PCC was calculated using an in-house tool written in Python. The PCCs were calculated in two different regions (pyrrole water and around C-propionate), as shown in fig. S21.

Time-resolved fluorescence experiments

Time-resolved fluorescence experiments were performed using a broadband fluorescence up-conversion instrument described in detail in (*95*). The setup uses a standard 1-kHz Ti:Sapphire amplified system (Coherent Astrella) producing 90-fs pulses at 800 nm as the main laser source. Excitation at 620 nm was achieved using an output from an in-house assembled two-stage noncollinear optical parametric amplifier pumped with the amplified laser system and subsequently compressed using a prism compressor. Polarization and intensity of the excitation pulses were controlled using a combination of a wire-grid polarizer and a half-waveplate. All measurements were performed at magic angle (54.7°) polarization with an excitation power of ~0.2 mW (200 nJ/pulse). The excitation pulses were focused down to a 100-µm spot at the sample resulting in an excitation intensity of ~0.025 mJ/mm^2. The gate pulses at 1345 nm were produced by an in-house assembled optical parametric amplifier and subsequently compressed using a prism compressor. Time resolution of the setup was estimated from the cross-correlation signal between the pump and gate pulses and was determined to be around 100 fs (full-width at half-maximum). The measurements were performed using a flow cell with an optical path length of about 400 µm. The sample was circulated through the cell with the use of a peristaltic pump. Before reentering the cell, the solution was illuminated with a 780-nm continuous wave laser to revert any possibly formed Pfr state back to the initial Pr state. The concentration of the samples was adjusted to have an absorption of about 0.2 to 0.4 at the excitation wavelength of 620 nm. The data were analyzed using a global lifetime analysis assuming a multiexponential decay kinetics.

Time-resolved IR spectroscopy

All transient IR spectra were measured in buffered D_2O. Concentrated HCl in H_2O was used to adjust the pH of 30 mM tris in D_2O to pH ~8 (measured with a standard glass electrode), and this corresponds to a pD of about 8.4 (*96*). The buffer was exchanged through repeated dilution and concentration with Amicon Ultra 10K MWCO centrifugal filters (Merck). The protein was switched between Pr and Pfr in ~5-min intervals for 1 hour, to enhance H/D exchange in both states and in intermediates. Laser diodes at ~655 and ~780 nm were used for illumination. Pump-probe IR measurements were performed as previously described (*65*).

All samples were measured at a room temperature of 21°C. The sample concentration was ~0.4 to 0.9 mM, and a closed-cycle flow-cell with CaF_2 windows, separated with a Teflon spacer at a path length of 50 µm, was used to circulate the sample (*97*). A flow rate of ~1.5 ml/min was enough to ensure complete sample exchange at ~1-kHz repetition rate. To keep the protein in the Pr state, the

sample was continuously illuminated with a light-emitting diode at ~780 nm (~10 mW) at a sample reservoir. In addition, the flow cell system was covered, and only dim light was used in the laboratory.

The pump-probe setup, which has been described earlier (*98*, *99*), was based on a 1-kHz Ti:Sapphire laser (Quantronix). The chromophore was excited with visible pump pulses ($\lambda = 692$ nm, duration = 150 fs, energy = 500 nJ, diameter = 300 μm). These visible pulses were generated by a TOPAS (traveling-wave optical parametric amplifier of superfluorescence; LIGHT CONVERSION, Inc.). Probe pulses in the mid-IR region (150 fs, 150-μm diameter) were obtained through an optical parametric amplifier (*100*). Both beams were focused on the same spot at the sample. In addition, a reference probe beam without visible excitation as well as an ~500-kHz chopper in the pump beam were used to obtain the transient IR spectra. The probe beams were dispersed in a spectrograph and detected with a 2×64 channel double-array HgCdTe detector (Infrared Systems Development). This setup has been described in more detail in (*98*). Several overlapping spectral windows (of ~100 cm^{-1}) between 1450 and 1750 cm^{-1} were recorded. The spectral positions were calibrated using waterlines, and the spectral resolution was about 4 cm^{-1} based on the width of the waterlines. The data were merged by scaling the different windows to the same intensity and averaging the data.

Data availability

The Coherent X-ray Imaging Data Bank ID 220 has all the relevant SX data related to this manuscript. The structural models will be made available through the PDB with accession codes 8C3I, 7GQV, 7GQW, 7GQX, 7GQY, 7GQZ, 7GR0, 7GR1, 7GR2, 7GR3, 7GR4, 7GR5, 7GR6, 7GR7, 7GR8, 7GR9, 7GRA, 7GRB, 7GRC, and 7GRD.

Supplementary Materials

The PDF file includes:
Tables S1 to S3
Figs. S1 to S26
Legend for movie S1

Other Supplementary Material for this manuscript includes the following:
Movie S1

REFERENCES AND NOTES

1. S. W. Lin, G. G. Kochendoerfer, K. S. Carroll, D. Wang, R. A. Mathies, T. P. Sakmar, Mechanisms of spectral tuning in blue cone visual pigments. Visible and raman spectroscopy of blue-shifted rhodopsin mutants. *J. Biol. Chem.* **273**, 24583–24591 (1998).
2. T. Gruhl, T. Weinert, M. J. Rodrigues, C. J. Milne, G. Ortolani, K. Nass, E. Nango, S. Sen, P. J. M. Johnson, C. Cirelli, A. Furrer, S. Mous, P. Skopintsev, D. James, F. Dworkowski, P. Båth, D. Kekilli, D. Ozerov, R. Tanaka, H. Glover, C. Bacellar, S. Brünle, C. M. Casadei, A. D. Diethelm, D. Gashi, G. Gotthard, R. Guixà-González, Y. Joti, V. Kabanova, G. Knopp, E. Lesca, P. Ma, I. Martiel, J. Mühle, S. Owada, F. Pamula, D. Sarabi, O. Tejero, C.-J. Tsai, N. Varma, A. Wach, S. Boutet, K. Tono, P. Nogly, X. Deupi, S. Iwata, R. Neutze, J. Standfuss, G. Schertler, V. Panneels, Ultrafast structural changes direct the first molecular events of vision. *Nature* **615**, 939–944 (2023).
3. G. Brändén, R. Neutze, Advances and challenges in time-resolved macromolecular crystallography. *Science* **373**, eaba0954 (2021).
4. K. Pande, C. D. M. M. Hutchison, G. Groenhof, A. Aquila, J. S. Robinson, J. Tenboer, S. Basu, S. Boutet, D. P. DePonte, M. Liang, T. A. White, N. A. Zatsepin, O. Yefanov, D. Morozov, D. Oberthuer, C. Gati, G. Subramanian, D. James, Y. Zhao, J. Koralek, J. Brayshaw, C. Kupitz, C. Conrad, S. Roy-Chowdhury, J. D. Coe, M. Metz, P. L. Xavier, T. D. Grant, J. E. Koglin, G. Ketawala, R. Fromme, V. Srajer, R. Henning, J. C. H. Spence, A. Ourmazd, P. Schwander, U. Weierstall, M. Frank, P. Fromme, A. Barty, H. N. Chapman, K. Moffat, J. J. van Thor, M. Schmidt, V. Šrajer, R. Henning, J. C. H. Spence, A. Ourmazd, P. Schwander, U. Weierstall, M. Frank, P. Fromme, A. Barty, H. N. Chapman, K. Moffat, J. J. van Thor, M. Schmidt, Femtosecond structural dynamics drives the trans/cis isomerization in photoactive yellow protein. *Science* **352**, 725–729 (2016).
5. P. Nogly, T. Weinert, D. James, S. Carbajo, D. Ozerov, A. Furrer, D. Gashi, V. Borin, P. Skopintsev, K. Jaeger, K. Nass, P. Båth, R. Bosman, J. Koglin, M. Seaberg, T. Lane, D. Kekilli, S. Brünle, T. Tanaka, W. Wu, C. Milne, T. White, A. Barty, U. Weierstall, V. Panneels, E. Nango, S. Iwata, M. Hunter, I. Schapiro, G. Schertler, R. Neutze, J. Standfuss, Retinal isomerization in bacteriorhodopsin captured by a femtosecond x-ray laser. *Science* **361**, eaat0094 (2018).
6. E. Claesson, W. Y. Wahlgren, H. Takala, S. Pandey, L. Castillon, V. Kuznetsova, L. Henry, M. Panman, M. Carrillo, J. Kübel, R. Nanekar, L. Isaksson, A. Nimmrich, A. Cellini, D. Morozov, M. Maj, M. Kurttila, R. Bosman, E. Nango, R. Tanaka, T. Tanaka, L. Fangjia, S. Iwata, S. Owada, K. Moffat, G. Groenhof, E. A. Stojković, J. A. Ihalainen, M. Schmidt, S. Westenhoff, The primary structural photoresponse of phytochrome proteins captured by a femtosecond x-ray laser. *eLife* **9**, e53514 (2020).
7. H. Wang, S. Lin, J. P. Allen, J. C. Williams, S. Blankert, C. Laser, N. W. Woodbury, Protein dynamics control the kinetics of initial electron transfer in photosynthesis. *Science* **316**, 747–750 (2007).
8. S. Sil, R. W. Tilluck, N. Mohan T. M., C. H. Leslie, J. B. Rose, M. A. Domínguez-Martín, W. Lou, C. A. Kerfeld, W. F. Beck, Excitation energy transfer and vibronic coherence in intact phycobilisomes. *Nat. Chem.* **14**, 1286–1294 (2022).
9. S. Tahara, R. Kurihara, K. Kojima, H. Kuramochi, S. Takeuchi, Y. Sudo, T. Tahara, Ultrafast protein dynamics prior to retinal photoisomerization in microbial rhodopsins. *J. Phys. Chem. Lett.* **16**, 5732–5738 (2025).
10. J. K. Yu, R. Liang, F. Liu, T. J. Martínez, First-principles characterization of the elusive I fluorescent state and the structural evolution of retinal protonated Schiff base in bacteriorhodopsin. *J. Am. Chem. Soc.* **141**, 18193–18203 (2019).
11. G. Nass Kovacs, J. P. Colletier, M. L. Grünbein, Y. Yang, T. Stensitzki, A. Batyuk, S. Carbajo, R. B. Doak, D. Ehrenberg, L. Foucar, R. Gasper, A. Gorel, M. Hilpert, M. Kloos, J. E. Koglin, J. Reinstein, C. M. Roome, R. Schlesinger, M. Seaberg, R. L. Shoeman, M. Stricker, S. Boutet, S. Haacke, J. Heberle, K. Heyne, T. Domratcheva, T. R. M. Barends, I. Schlichting, Three-dimensional view of ultrafast dynamics in photoexcited bacteriorhodopsin. *Nat. Commun.* **10**, 3177 (2019).
12. T. Stensitzki, S. Adam, R. Schlesinger, I. Schapiro, K. Heyne, Ultrafast backbone protonation in channelrhodopsin-1 captured by polarization resolved Fs Vis-pump—IR-probe spectroscopy and computational methods. *Molecules* **25**, 848 (2020).
13. J. Cao, R. J. Cogdell, D. F. Coker, H.-G. G. Duan, J. Hauer, U. Kleinekathöfer, T. L. C. Jansen, T. Mančal, R. J. D. Miller, J. P. Ogilvie, V. I. Prokhorenko, T. Renger, H.-S. Tan, R. Tempelaar, M. Thorwart, E. Thyrhaug, S. Westenhoff, D. Zigmantas, Quantum biology revisited. *Sci. Adv.* **6**, eaaz4888 (2020).
14. G. D. Scholes, G. R. Fleming, L. X. Chen, A. Aspuru-Guzik, A. Buchleitner, D. F. Coker, G. S. Engel, R. Van Grondelle, A. Ishizaki, D. M. Jonas, J. S. Lundeen, J. K. McCusker, S. Mukamel, J. P. Ogilvie, A. Olaya-Castro, M. A. Ratner, F. C. Spano, K. B. Whaley, X. Zhu, Using coherence to enhance function in chemical and biophysical systems. *Nature* **543**, 647–656 (2017).
15. A. Migliore, N. F. Polizzi, M. J. Therien, D. N. Beratan, Biochemistry and theory of proton-coupled electron transfer. *Chem. Rev.* **114**, 3381–3465 (2014).
16. M. Chattoraj, B. A. King, G. U. Bublitz, S. G. Boxer, Ultra-fast excited state dynamics in green fluorescent protein: Multiple states and proton transfer. *Proc. Natl. Acad. Sci. U.S.A.* **93**, 8362–8367 (1996).
17. A. P. Demchenko, Proton transfer reactions: From photochemistry to biochemistry and bioenergetics. *BBA Advances* **3**, 100085 (2023).
18. G. A. Parada, Z. K. Goldsmith, S. Kolmar, B. P. Rimgard, B. Q. Mercado, L. Hammarström, S. Hammes-Schiffer, J. M. Mayer, Concerted proton-electron transfer reactions in the Marcus inverted region. *Science* **364**, 471–475 (2019).
19. Y. Yang, T. Stensitzki, L. Sauthof, A. Schmidt, P. Piwowarski, F. Velazquez Escobar, N. Michael, A. D. Nguyen, M. Szczepek, F. N. Brünig, R. R. Netz, M. A. Mroginski, S. Adam, F. Bartl, I. Schapiro, P. Hildebrandt, P. Scheerer, K. Heyne, Ultrafast proton-coupled isomerization in the phototransformation of phytochrome. *Nat. Chem.* **14**, 823–830 (2022).
20. P. Goyal, S. Hammes-Schiffer, Role of active site conformational changes in photocycle activation of the AppA BLUF photoreceptor. *Proc. Natl. Acad. Sci. U.S.A.* **114**, 1480–1485 (2017).
21. J. J. van Thor, P. M. Champion, Photoacid dynamics in the green fluorescent protein. *Annu. Rev. Phys. Chem.* **74**, 123–144 (2023).
22. W. L. Butler, K. H. Norris, H. W. Siegelman, S. B. Hendricks, Detection, assay, and preliminary purification of the pigment controlling photoresponsive development of plants. *Proc. Natl. Acad. Sci. U.S.A.* **45**, 1703–1708 (1959).
23. M. Legris, Y. Ç. Ince, C. Fankhauser, Molecular mechanisms underlying phytochrome-controlled morphogenesis in plants. *Nat. Commun.* **10**, 5219 (2019).
24. X. Shu, A. Royant, M. Z. Lin, T. A. Aguilera, V. Lev-Ram, P. A. Steinbach, R. Y. Tsien, Mammalian expression of infrared fluorescent proteins engineered from a bacterial phytochrome. *Science* **324**, 804–807 (2009).
25. W. Y. Wahlgren, E. Claesson, I. Tuure, S. Trillo-Muyo, S. Bódizs, J. A. Ihalainen, H. Takala, S. Westenhoff, Structural mechanism of signal transduction in a phytochrome histidine kinase. *Nat. Commun.* **13**, 7673 (2022).

26. L.-O. Essen, J. Mailliet, J. Hughes, The structure of a complete phytochrome sensory module in the Pr ground state. *Proc. Natl. Acad. Sci. U.S.A.* **105**, 14709–14714 (2008).
27. H. Li, E. S. Burgie, Z. T. K. Gannam, H. Li, R. D. Vierstra, Plant phytochrome B is an asymmetric dimer with unique signalling potential. *Nature* **604**, 127–133 (2022).
28. X. Yang, J. Kuk, K. Moffat, Crystal structure of *Pseudomonas aeruginosa* bacteriophytochrome: Photoconversion and signal transduction. *Proc. Natl. Acad. Sci. U.S.A.* **105**, 14715–14720 (2008).
29. H. Takala, A. Björling, O. Berntsson, H. Lehtivuori, S. Niebling, M. Hoernke, I. Kosheleva, R. Henning, A. Menzel, J. A. Ihalainen, S. Westenhoff, Signal amplification and transduction in phytochrome photosensors. *Nature* **509**, 245–248 (2014).
30. J. J. van Thor, K. L. Ronayne, M. Towrie, Formation of the early photoproduct Lumi-R of cyanobacterial phytochrome Cph1 observed by ultrafast mid-infrared spectroscopy. *J. Am. Chem. Soc.* **129**, 126–132 (2007).
31. J. Dasgupta, R. R. Frontiera, K. C. Taylor, J. C. Lagarias, R. A. Mathies, Ultrafast excited-state isomerization in phytochrome revealed by femtosecond stimulated Raman spectroscopy. *Proc. Natl. Acad. Sci. U.S.A.* **106**, 1784–1789 (2009).
32. D. Buhrke, N. Michael, P. Hamm, Vibrational couplings between protein and cofactor in bacterial phytochrome Agp1 revealed by 2D-IR spectroscopy. *Proc. Natl. Acad. Sci. U.S.A.* **119**, (2022).
33. M. Chenchiliyan, J. Kübel, S. A. Ooi, G. Salvadori, B. Mennucci, S. Westenhoff, M. Maj, Ground-state heterogeneity and vibrational energy redistribution in bacterial phytochrome observed with femtosecond 2D IR spectroscopy. *J. Chem. Phys.* **158**, 085103 (2023).
34. M. G. Müller, I. Lindner, I. Martin, W. Gärtner, A. R. Holzwarth, Femtosecond kinetics of photoconversion of the higher plant photoreceptor phytochrome carrying native and modified chromophores. *Biophys. J.* **94**, 4370–4382 (2008).
35. Y. Yang, M. Linke, T. Von Haimberger, J. Hahn, R. Matute, L. González, P. Schmieder, K. Heyne, Real-time tracking of phytochrome's orientational changes during Pr photoisomerization. *J. Am. Chem. Soc.* **134**, 1408–1411 (2012).
36. C. Slavov, T. Fischer, A. Barnoy, H. Shin, A. G. Rao, C. Wiebeler, X. Zeng, Y. Sun, Q. Xu, A. Gutt, K. H. Zhao, W. Gärtner, X. Yang, I. Schapiro, J. Wachtveitl, The interplay between chromophore and protein determines the extended excited state dynamics in a single-domain phytochrome. *Proc. Natl. Acad. Sci. U.S.A.* **117**, 16356–16362 (2020).
37. Y. Yang, M. Linke, T. von Haimberger, R. Matute, L. González, P. Schmieder, K. Heyne, Active and silent chromophore isoforms for phytochrome Pr photoisomerization: An alternative evolutionary strategy to optimize photoreaction quantum yields. *Struct. Dyn.* **1**, 014701 (2014).
38. P. W. Kim, N. C. Rockwell, S. S. Martin, J. C. Lagarias, D. S. Larsen, Dynamic inhomogeneity in the photodynamics of cyanobacterial phytochrome cph1. *Biochemistry* **53**, 2818–2826 (2014).
39. M. Linke, Y. Yang, B. Zienicke, M. A. S. Hammam, T. Von Haimberger, A. Zacarias, K. Inomata, T. Lamparter, K. Heyne, Electronic transitions and heterogeneity of the bacteriophytochrome Pr absorption band: An angle balanced polarization resolved femtosecond VIS pump-IR probe study. *Biophys. J.* **105**, 1756–1766 (2013).
40. P. W. Kim, N. C. Rockwell, L. H. Freer, C. W. Chang, S. S. Martin, J. C. Lagarias, D. S. Larsen, Unraveling the primary isomerization dynamics in cyanobacterial phytochrome Cph1 with multipulse manipulations. *J. Phys. Chem. Lett.* **4**, 2605–2609 (2013).
41. G. Salvadori, V. Macaluso, G. Pellicci, L. Cupellini, G. Granucci, B. Mennucci, Protein control of photochemistry and transient intermediates in phytochromes. *Nat. Commun.* **13**, 6838 (2022).
42. D. Morozov, V. Modi, V. Mironov, G. Groenhof, The photocycle of bacteriophytochrome is initiated by counterclockwise chromophore isomerization. *J. Phys. Chem. Lett.* **13**, 4538–4542 (2022).
43. R. Dods, P. Båth, D. Morozov, V. A. Gagnér, D. Arnlund, H. L. Luk, J. Kübel, M. Maj, A. Vallejos, C. Wickstrand, R. Bosman, K. R. Beyerlein, G. Nelson, M. Liang, D. Milathianaki, J. Robinson, R. Harimoorthy, P. Berntsen, E. Malmerberg, L. Johansson, R. Andersson, S. Carbajo, E. Claesson, C. E. Conrad, P. Dahl, G. Hammarin, M. S. Hunter, C. Li, S. Lisova, A. Royant, C. Safari, A. Sharma, G. J. Williams, O. Yefanov, S. Westenhoff, J. Davidsson, D. P. DePonte, S. Boutet, A. Barty, G. Katona, G. Groenhof, G. Brändén, R. Neutze, Ultrafast structural changes within a photosynthetic reaction centre. *Nature* **589**, 310–314 (2021).
44. K. C. Toh, E. A. Stojkovic, I. H. M. van Stokkum, K. Moffat, J. T. M. Kennis, E. A. Stojković, I. H. M. van Stokkum, K. Moffat, J. T. M. Kennis, Proton-transfer and hydrogen-bond interactions determine fluorescence quantum yield and photochemical efficiency of bacteriophytochrome. *Proc. Natl. Acad. Sci. U.S.A.* **107**, 9170–9175 (2010).
45. M. Carrillo, S. Pandey, J. Sanchez, M. Noda, I. Poudyal, L. Aldama, T. N. Malla, E. Claesson, W. Y. Wahlgren, D. Feliz, V. Šrajer, M. Maj, L. Castillon, S. Iwata, E. Nango, R. Tanaka, T. Tanaka, L. Fangjia, K. Tono, S. Owada, S. Westenhoff, E. A. Stojković, M. Schmidt, High-resolution crystal structures of transient intermediates in the phytochrome photocycle. *Structure* **29**, 743–754.e4 (2021).
46. A. Schmidt, L. Sauthof, M. Szczepek, M. F. Lopez, F. V. Escobar, B. M. Qureshi, N. Michael, D. Buhrke, T. Stevens, D. Kwiatkowski, D. von Stetten, M. A. Mroginski, N. Krauß, T. Lamparter, P. Hildebrandt, P. Scheerer, Structural snapshot of a bacterial phytochrome in its functional intermediate state. *Nat. Commun.* **9**, 4912 (2018).
47. T. R. M. Barends, A. Gorel, S. Bhattacharyya, G. Schirò, C. Bacellar, C. Cirelli, J.-P. Colletier, L. Foucar, M. L. Grünbein, E. Hartmann, M. Hilpert, J. M. Holton, P. J. M. Johnson, M. Kloos, G. Knopp, B. Marekha, K. Nass, G. Nass Kovacs, D. Ozerov, M. Stricker, M. Weik, R. B. Doak, R. L. Shoeman, C. J. Milne, M. Huix-Rotllant, M. Cammarata, I. Schlichting, Influence of pump laser fluence on ultrafast myoglobin structural dynamics. *Nature* **626**, 905–911 (2024).
48. A. G. Rao, C. Wiebeler, S. Sen, D. S. Cerutti, I. Schapiro, Histidine protonation controls structural heterogeneity in the cyanobacteriochrome AnPixJg2. *Phys. Chem. Chem. Phys.* **23**, 12494 (2021).
49. A. Takiden, F. Velazquez-Escobar, J. Dragelj, A. L. Woelke, E. Knapp, P. Piwowarski, F. Bart, P. Hildebrandt, M. A. Mroginski, Structural and vibrational characterization of the chromophore binding site of bacterial phytochrome Agp1. *Photochem. Photobiol.* **93**, 713–723 (2017).
50. J. Wang, W. Wang, P. A. Kollman, D. A. Case, Automatic atom type and bond type perception in molecular mechanical calculations. *J. Mol. Graph. Model.* **25**, 247–260 (2006).
51. N. Lenngren, P. Edlund, H. Takala, B. Stucki-Buchli, J. Rumfeldt, I. Peshev, H. Häkkänen, S. Westenhoff, J. A. Ihalainen, Coordination of the biliverdin D-ring in bacteriophytochromes. *Phys. Chem. Chem. Phys.* **20**, 18216–18225 (2018).
52. A. Barth, The infrared absorption of amino acid side chains. *Prog. Biophys. Mol. Biol.* **74**, 141–173 (2000).
53. T. N. Do, D. Menendez, D. Bizhga, E. A. Stojković, J. T. M. Kennis, Two-photon absorption and photoionization of a bacterial phytochrome. *J. Mol. Biol.* **168357**, (2023).
54. T. N. Malla, L. Aldama, V. Leon, D. Feliz, H. Hu, I. Thomas, A. Cellini, W. Y. Wahlgren, A. Nimmrich, S. Botha, R. Sierra, M. S. Hunter, F. Poitevin, S. Lisova, A. Batyuk, G. Gate, R. Jernigan, C. J. Kupitz, P. Maj, P. Meszaros, M. Kurttila, L. Monrroy, F. Luo, S. Owada, J. Kang, C. Slavov, M. Maj, C. Gautier, M. Kashipathy, A. Tolstikova, V. Mariani, A. Barty, F. Moss, P. Schwander, H. Liu, S. Boutet, P. Fromme, H. Takala, J. A. Ihalainen, U. Weierstall, S. Westenhoff, E. A. Stojković, M. Schmidt, Observation of early events in the photoactivation of Myxobacterial phytochrome using time-resolved serial femtosecond crystallography. *Commun. Chem.* **8**, 183 (2025).
55. S. Perrett, A. Fadini, C. D. M. Hutchison, H. Rycroft, S. Bhattacharya, D. Morozov, S. Muniyappan, T. N. Malla, D. Khakhulin, O. Turkot, H. Yousef, J. Valerio, M. B. Jakobsen, M. Biednov, Y. Jiang, H. Ha, F. Dall'Antonia, D. Vinci, M. Größler, J. Licón-Saláiz, F. Griese, S. Flewett, J. Schulz, A. Barty, C. Milne, M. Schmidt, G. Groenhof, J. J. van Thor, Crystal optics select weak response of ultrafast crystallography of the Photoactive Yellow Protein. *ChemRxiv* 10.26434/chemrxiv-2025-72m69 (2025).
56. K. Heyne, Impact of ultrafast electric field changes on photoreceptor protein dynamics. *J. Phys. Chem. B* **126**, 581–587 (2022).
57. S. Schenkl, F. van Mourik, G. van der Zwan, S. Haacke, M. Chergui, Probing the ultrafast charge translocation of photoexcited retinal in bacteriorhodopsin. *Science* **309**, 917–920 (2005).
58. C.-Y. Huang, S. He, W. F. DeGrado, D. G. McCafferty, F. Gai, Light-induced helix formation. *J. Am. Chem. Soc.* **124**, 12674–12675 (2002).
59. Y. Yang, T. Stensitzki, C. Lang, J. Hughes, M. A. Mroginski, K. Heyne, Ultrafast protein response in the Pfr state of Cph1 phytochrome. *Photochem. Photobiol. Sci.* **22**, 919–930 (2023).
60. M. Theiß, M. Grupe, T. Lamparter, M. A. Mroginski, R. Diller, Ultrafast proton release reaction and primary photochemistry of phycocyanobilin in solution observed with fs-time-resolved mid-IR and UV/Vis spectroscopy. *Photochem. Photobiol. Sci.* **20**, 715–732 (2021).
61. J. A. Rumfeldt, H. Takala, A. Liukkonen, J. A. Ihalainen, UV-Vis spectroscopy reveals a correlation between Y263 and BV protonation states in bacteriophytochromes. *Photochem. Photobiol.* **95**, 969–979 (2019).
62. H. Lehtivuori, J. Rumfeldt, S. Mustalahti, S. Kurkinen, H. Takala, Conserved histidine and tyrosine determine spectral responses through the water network in *Deinococcus radiodurans* phytochrome. *Photochem. Photobiol. Sci.* **21**, 1975–1989 (2022).
63. J. R. Wagner, J. Zhang, D. von Stetten, M. Günther, D. H. Murgida, M. A. Mroginski, J. M. Walker, K. T. Forest, P. Hildebrandt, R. D. Vierstra, Mutational analysis of *Deinococcus radiodurans* bacteriophytochrome reveals key amino acids necessary for the photochromicity and proton exchange cycle of phytochromes. *J. Biol. Chem.* **283**, 12212–12226 (2008).
64. M. Levantino, G. Schirò, H. T. Lemke, G. Cottone, J. M. Glownia, D. Zhu, M. Chollet, H. Ihee, A. Cupane, M. Cammarata, Ultrafast myoglobin structural dynamics observed with an X-ray free-electron laser. *Nat. Commun.* **6**, 6772 (2015).
65. J. A. Ihalainen, E. Gustavsson, L. Schroeder, S. Donnini, H. Lehtivuori, L. Isaksson, C. Thöing, V. Modi, O. Berntsson, B. Stucki-Buchli, A. Liukkonen, H. Häkkänen, E. Kalenius, S. Westenhoff, T. Kottke, Chromophore–protein interplay during the phytochrome photocycle revealed by step-scan FTIR spectroscopy. *J. Am. Chem. Soc.* **140**, 12396–12404 (2018).
66. T. Kameshima, S. Ono, T. Kudo, K. Ozaki, Y. Kirihara, K. Kobayashi, Y. Inubushi, M. Yabashi, T. Horigome, A. Holland, K. Holland, D. Burt, H. Murao, T. Hatsui, Development of an X-ray pixel detector with multi-port charge-coupled device for X-ray free-electron laser experiments. *Rev. Sci. Instrum.* **85**, (2014).
67. T. Nakane, Y. Joti, K. Tono, M. Yabashi, E. Nango, S. Iwata, R. Ishitani, O. Nureki, Data processing pipeline for serial femtosecond crystallography at SACLA. *J. Appl. Cryst.* **49**, 1035–1041 (2016).

68. A. Barty, R. A. Kirian, F. R. N. C. Maia, M. Hantke, C. H. Yoon, T. A. White, H. Chapman, Cheetah: Software for high-throughput reduction and analysis of serial femtosecond X-ray diffraction data. *J. Appl. Cryst.* **47**, 1118–1131 (2014).
69. T. A. White, Processing serial crystallography data with CrystFEL: A step-by-step guide. *Acta Crystallogr. D Struct. Biol.* **75** (Pt. 2), 219–233 (2019).
70. T. Sato, T. Togashi, K. Ogawa, T. Katayama, Y. Inubushi, K. Tono, M. Yabashi, Highly efficient arrival timing diagnostics for femtosecond X-ray and optical laser pulses. *Appl. Phys. Express* **8**, 012702 (2015).
71. Z. Ren, B. Perman, V. Šrajer, T.-Y. Teng, C. Pradervand, D. Bourgeois, F. Schotte, T. Ursby, R. Kort, M. Wulff, K. Moffat, A molecular movie at 1.8 Å resolution displays the photocycle of photoactive yellow protein, a eubacterial blue-light receptor, from nanoseconds to seconds. *Biochemistry* **40**, 13788–13801 (2001).
72. M. D. Winn, C. C. Ballard, K. D. Cowtan, E. J. Dodson, P. Emsley, P. R. Evans, R. M. Keegan, E. B. Krissinel, A. G. W. Leslie, A. McCoy, S. J. McNicholas, G. N. Murshudov, N. S. Pannu, E. A. Potterton, H. R. Powell, R. J. Read, A. Vagin, K. S. Wilson, Overview of the *CCP* 4 suite and current developments. *Acta Crystallogr. D Biol. Crystallogr.* **67**, 235–242 (2011).
73. D. Liebschner, P. V. Afonine, M. L. Baker, G. Bunkoczi, V. B. Chen, T. I. Croll, B. Hintze, L. W. Hung, S. Jain, A. J. McCoy, N. W. Moriarty, R. D. Oeffner, B. K. Poon, M. G. Prisant, R. J. Read, J. S. Richardson, D. C. Richardson, M. D. Sammito, O. V. Sobolev, D. H. Stockwell, T. C. Terwilliger, A. G. Urzhumtsev, L. L. Videau, C. J. Williams, P. D. Adams, Macromolecular structure determination using X-rays, neutrons and electrons: Recent developments in Phenix. *Acta Crystallogr. D Struct. Biol.* **75**, 861–877 (2019).
74. P. Emsley, B. Lohkamp, W. G. Scott, K. Cowtan, Features and development of *Coot*. *Acta Crystallogr. D Biol. Crystallogr.* **66**, 486–501 (2010).
75. S. Pandey, R. Bean, T. Sato, I. Poudyal, J. Bielecki, J. Cruz Villarreal, O. Yefanov, V. Mariani, T. A. White, C. Kupitz, M. Hunter, M. H. Abdellatif, S. Bajt, V. Bondar, A. Echelmeier, D. Doppler, M. Emons, M. Frank, R. Fromme, Y. Gevorkov, G. Giovanetti, M. Jiang, D. Kim, Y. Kim, H. Kirkwood, A. Klimovskaia, J. Knoska, F. H. M. Koua, R. Letrun, S. Lisova, L. Maia, V. Mazalova, D. Meza, T. Michelat, A. Ourmazd, G. Palmer, M. Ramilli, R. Schubert, P. Schwander, A. Silenzi, J. Sztuk-Dambietz, A. Tolstikova, H. N. Chapman, A. Ros, A. Barty, P. Fromme, A. P. Mancuso, M. Schmidt, Time-resolved serial femtosecond crystallography at the European XFEL. *Nat. Methods* **17**, 73–78 (2020).
76. R. Henderson, J. K. Moffat, The difference Fourier technique in protein crystallography: Errors and their treatment. *Acta Crystallogr. B* **27**, 1414–1420 (1971).
77. R. Sánchez, A. Sali, Large-scale protein structure modeling of the *Saccharomyces cerevisiae* genome. *Proc. Natl. Acad. Sci.* **95**, 13597–13602 (1998).
78. R. Anandakrishnan, B. Aguilar, A. V. Onufriev, *H*++ 3.0: Automating p*K* prediction and the preparation of biomolecular structures for atomistic molecular modeling and simulations. *Nucleic Acids Res.* **40**, W537–W541 (2012).
79. E. Maximowitsch, Molecular mechanisms of spectral tuning and excited-state decay in phytochrome photoreceptors, thesis, University Heidelberg, Heidelberg (2019).
80. J. A. Maier, C. Martinez, K. Kasavajhala, L. Wickstrom, K. E. Hauser, C. Simmerling, ff14SB: Improving the accuracy of protein side chain and backbone parameters from ff99SB. *J. Chem. Theory Comput.* **11**, 3696–3713 (2015).
81. V. Modi, S. Donnini, G. Groenhof, D. Morozov, Protonation of the biliverdin IXα chromophore in the red and far-red photoactive states of a bacteriophytochrome. *J. Phys. Chem. B* **123**, 2325–2334 (2019).
82. V. Macaluso, L. Cupellini, G. Salvadori, F. Lipparini, B. Mennucci, Elucidating the role of structural fluctuations, and intermolecular and vibronic interactions in the spectroscopic response of a bacteriophytochrome. *Phys. Chem. Chem. Phys.* **22**, 8585–8594 (2020).
83. T. Yanai, D. P. Tew, N. C. Handy, A new hybrid exchange–correlation functional using the Coulomb-attenuating method (CAM-B3LYP). *Chem. Phys. Lett.* **393**, 51–57 (2004).
84. B. Mennucci, J. Tomasi, Continuum solvation models: A new approach to the problem of solute's charge distribution and cavity boundaries. *Journal of Chemical Physics* **106**, (1997).
85. J. S. Hub, B. L. de Groot, H. Grubmüller, G. Groenhof, Quantifying artifacts in Ewald simulations of inhomogeneous systems with a net charge. *J. Chem. Theory Comput.* **10**, 381–390 (2014).
86. D. A. Case, H. M. Aktulga, K. Belfon, D. S. Cerutti, G. A. Cisneros, V. W. D. Cruzeiro, N. Forouzesh, T. J. Giese, A. W. Götz, H. Gohlke, S. Izadi, K. Kasavajhala, M. C. Kaymak, E. King, T. Kurtzman, T.-S. Lee, P. Li, J. Liu, T. Luchko, R. Luo, M. Manathunga, M. R. Machado, H. M. Nguyen, K. A. O'Hearn, A. V. Onufriev, F. Pan, S. Pantano, R. Qi, A. Rahnamoun, A. Risheh, S. Schott-Verdugo, A. Shajan, J. Swails, J. Wang, H. Wei, X. Wu, Y. Wu, S. Zhang, S. Zhao, Q. Zhu, T. E. Cheatham, D. R. Roe, A. Roitberg, C. Simmerling, D. M. York, M. C. Nagan, K. M. Merz, AmberTools. *J. Chem. Inf. Model.* **63**, 6183–6191 (2023).
87. W. L. Jorgensen, J. Chandrasekhar, J. D. Madura, R. W. Impey, M. L. Klein, Comparison of simple potential functions for simulating liquid water. *J. Chem. Phys.* **79**, 926–935 (1983).
88. H. G. Wallnoefer, K. R. Liedl, T. Fox, A challenging system: Free energy prediction for factor Xa. *J. Comput. Chem.* **32**, 1743–1752 (2011).
89. J. Roe, C. Thompson, P. Aspinall, M. Brewer, E. Duff, D. Miller, R. Mitchell, A. Clow, Green space and stress: Evidence from cortisol measures in deprived urban communities. *Int. J. Environ. Res. Public Health* **10**, 4086–4103 (2013).
90. C. I. Bayly, P. Cieplak, W. D. Cornell, P. A. Kollman, A well-behaved electrostatic potential based method using charge restraints for deriving atomic charges: The RESP model. *J. Phys. Chem.* **97**, 10269–10280 (1993).
91. D. A. Case, T. E. I. Cheatham, C. Simmerling, A. Roitberg, K. M. Merz, R. C. Walker, R. Luo, P. Li, T. Darden, C. Sagui, F. Pan, J. Wang, D. R. Roe, J. Swails, A. W. Götz, J. Smith, D. Cerutti, T. Lee, D. York, T. Giese, T. Luchko, N. Forouzesh, V. Man, V. W. D. Cruzeiro, G. Monard, Y. Miao, J. Wang, C. Lin, G. A. Cisneros, A. Rahnamoun, A. Shajan, M. Manathunga, J. T. Berryman, N. R. Skrynnikov, O. Mikhailovskii, Y. Xue, S. A. Izmailov, K. Kasavajhala, K. Belfon, J. Shen, J. Harris, A. Onufriev, S. Izadi, X. Wu, H. Gohlke, S. Schott-Verdugo, R. Qi, H. Wei, Y. Wu, S. Zhao, Q. Zhu, E. King, G. Giamba, J. Liu, H. Nguyen, S. R. Brozell, A. Kovalenko, M. Gilson, I. Ben-Shalom, T. Kurtzman, S. Pantano, M. Machado, H. M. Aktulga, M. C. Kaymak, K. A. O'Hearn, P. A. Kollman, *Amber 2023 Reference Manual* (University of California, 2023).
92. T. Schneider, E. Stoll, Molecular-dynamics study of a three-dimensional one-component model for distortive phase transitions. *Phys. Rev. B* **17**, 1302–1322 (1978).
93. H. J. C. Berendsen, J. P. M. Postma, W. F. van Gunsteren, A. DiNola, J. R. Haak, Molecular dynamics with coupling to an external bath. *J. Chem. Phys.* **81**, 3684–3690 (1984).
94. T. Darden, D. York, L. Pedersen, Particle mesh Ewald: An *N* ·log(*N*) method for Ewald sums in large systems. *J. Chem. Phys.* **98**, 10089–10092 (1993).
95. K. Pyo, M. F. Matus, E. Hulkko, P. Myllyperkiö, S. Malola, T. Kumpulainen, H. Häkkinen, M. Pettersson, Atomistic view of the energy transfer in a fluorophore-functionalized gold nanocluster. *J. Am. Chem. Soc.* **145**, 14697–14704 (2023).
96. A. K. Covington, M. Paabo, R. A. Robinson, R. G. Bates, Use of the glass electrode in deuterium oxide and the relation between the standardized pD (paD) scale and the operational pH in Heavy Water. *Anal. Chem.* **40**, 700–706 (1968).
97. J. Bredenbeck, P. Hamm, Versatile small volume closed-cycle flow cell system for transient spectroscopy at high repetition rates. *Review of Scientific Instruments* **74**, 3188–3189 (2003).
98. E. M. S. Maçôas, R. Kananavicius, P. Myllyperkiö, M. Pettersson, H. Kunttu, Ultrafast electronic and vibrational energy relaxation of Fe(acetylacetonate)3 in solution. *J. Phys. Chem. Lett.* **111**, 2054–2061 (2007).
99. S. Mustalahti, P. Myllyperkiö, T. Lahtinen, K. Salorinne, S. Malola, J. Koivisto, H. Häkkinen, M. Pettersson, Ultrafast electronic relaxation and vibrational cooling dynamics of $Au_{144}(SC_2H_4Ph)_{60}$ nanocluster probed by transient mid-IR spectroscopy. *J. Phys. Chem. C* **118**, 18233–18239 (2014).
100. P. Hamm, R. A. Kaindl, J. Stenger, Noise suppression in femtosecond mid-infrared light sources. *Opt. Lett.* **25**, 1798 (2000).
101. P. Hamm, Coherent effects in femtosecond infrared spectroscopy. *Chem. Phys.* **200**, 415–429 (1995).

Acknowledgments: The authors thank G. Groenhof (University of Jyväskylä) for providing the QM trajectories presented in Fig. 3 and figs. S25 and S26. **Funding:** S.W. acknowledges the European Research Council for support (grant number: 279944). M.S. acknowledges support by NSF-STC-1231306 (BioXFEL), J.A.I. by the Research Council of Finland grant 332742, H.T. by the Research Council of Finland grant 330678, and E.A.S. by the NSF-STC-123306 (BioXFEL) subaward 6227. M.S. and E.A.S are also supported by NSF-2423602. M.K.S. acknowledges the Karin and Herbert Jacobson Foundation for providing a postdoctoral scholarship and Längmanska Kulturfonden grant (BA23-0489) for funding. B.S.-B. acknowledges support through a postdoctoral grant by the Swiss National Science Foundation (P2ZHP2_164991). MD simulations were enabled by resources provided by the National Academic Infrastructure for Supercomputing in Sweden (NAISS) at NSC Tetralith and PDC Dardel. The experiments were performed at SACLA with the approval of JASRI and the program review committee (no. 2021A8002). The funders had no role in study design, data collection and analysis, decision to publish, or preparation of the manuscript. **Author contributions:** The overall study plan and experiment was conceptualized by S.W., J.A.I., and M.S. Protein crystals were prepared by W.Y.W., H.T., A.L.A., E.C., and P.M. The SX data processing and data analysis were carried out by S.W. and M.K.S. The MD study was performed by S.W. and L.G. A.-L.F. contributed analysis of the QM/MM simulations. M.K.S., W.Y.W., A.N., M.K., A.C., P.M., T.N.M., S.P., H.T., E.A.S., M.S., J.A.I., and S.W. performed the online experiment and analyzed the data at the experiment. F.L., T.T., N.N., R.T., K.T., and S.O. performed the experiments in person at the beamline BL3, SACLA, Japan. B.S.-B., T.K., P.M., and M.K. performed spectroscopic experiments. S.W., M.K.S., L.G., and J.A.I. wrote the paper with input from all authors. **Competing interests:** The authors declare that they have no competing interests. **Data and materials availability:** All data needed to evaluate the conclusions in the paper are present in the paper and/or the Supplementary Materials. The trajectories and parameters have been made available via Zenodo (10.5281/zenodo.17208598).

Submitted 7 April 2025
Accepted 18 September 2025
Published 17 October 2025
10.1126/sciadv.ady0499